UNIVERSIDADE FEDERAL DE UBERLÂNDIA

CARLOS ANTONIO RIBEIRO DUARTE

Numerical investigation of the erosion reduction in elbows promoted by a vortex chamber

Uberlândia – MG – Brasil

27 de Março de 2015

CARLOS ANTONIO RIBEIRO DUARTE

Numerical investigation of the erosion reduction in elbows promoted by a vortex chamber

Dissertação apresentada ao Programa de Pós-Graduação em Engenharia Mecânica da Universidade Federal de Uberlândia, como parte dos requisitos para a obtenção do título de **MESTRE EM ENGENHARIA MECÂNICA**.

Área de concentração: Transferência de Calor e Mecânica dos Fluidos

Universidade Federal de Uberlândia – UFU

Faculdade de Engenharia Mecânica

Programa de Pós-Graduação

Supervisor: Prof. Dr. Francisco José de Souza

Uberlândia – MG – Brasil

27 de Março de 2015

Dados Internacionais de Catalogação na Publicação (CIP)
Sistema de Bibliotecas da UFU, MG, Brasil.

D812n 2015

Duarte, Carlos Antonio Ribeiro, 1989 -
Numerical investigation of the erosion reduction in elbows promoted by a vortex chamber/ Carlos Antonio Ribeiro Duarte. – 2015.
95 f. : il.

Orientador: Francisco José de Souza
Dissertação (Mestrado) – Universidade Federal de Uberlândia , Programa de Pós-Graduação em Engenharia Mecânica.
Inclui bibliografia

1. Engenharia mecânica - Teses. 2. Desgaste mecânico - Teses. 3. Lagrange, Funções de - Teses. 4. Amortecimento (Mecânica) - Teses. I. Souza, Francisco José de. II. Universidade Federal de Uberlândia. III. Programa de Pós-Graduação em Engenharia Mecânica. IV. Título

CDU:621

CARLOS ANTONIO RIBEIRO DUARTE

Numerical investigation of the erosion reduction in elbows promoted by a vortex chamber

Dissertação apresentada ao Programa de Pós-Graduação em Engenharia Mecânica da Universidade Federal de Uberlândia, como parte dos requisitos para a obtenção do título de **MESTRE EM ENGENHARIA MECÂNICA**.

Área de concentração: Transferência de Calor e Mecânica dos Fluidos

Trabalho aprovado. Uberlândia – MG – Brasil, 27 de março de 2015:

Prof. Dr. Francisco José de Souza
Orientador - UFU

Prof. Aristeu da Silveira Neto, Dr. Ing.
UFU

Waldir Pedro Martignoni, Ph.D.
PETROBRAS

Uberlândia – MG – Brasil
27 de Março de 2015

To my family for always standing by my side.

Acknowledgements

I would like to express my gratitude to my supervisor, Prof. Dr. Francisco José de Souza, whose expertise, understanding, and patience, added considerably to my graduate experience. I appreciate his vast knowledge and skill in many areas and his assistance in writing reports (i.e., publications, conference papers and this dissertation).

A very special thanks goes out to Prof. Dr. Aristeu da Silveira Neto, without whose motivation and encouragement I would not have considered a graduate career mechanical engineering research. It was under his tutelage that I developed a focus and became interested in computational fluid dynamics. He provided me with direction, technical support and became more of a mentor and friend, than a professor. It was through his, persistence, understanding and kindness that I completed my undergraduate degree and was encouraged to apply for graduate training. I doubt that I will ever be able to convey my appreciation fully, but I owe him my eternal gratitude.

Thanks also goes out to those who provided me with technical advice at times of critical need; Msc. Bruno Tadeu, Msc. João Rodrigo and Vinicius Fagundes. I would also like to thank my friends at MFLab[1], for our philosophical debates, exchanges of knowledge, skills, and venting of frustration during my graduate program, which helped enrich the experience.

I would also like to thank my parents, Maria Beatriz and José Carlos for the support they provided me through my entire life, my brother Lucas Eduardo for the friendship and in particular, I must acknowledge my fiancée and best friend, Larissa, without whose love, encouragement and patience, I would not have finished this dissertation.

In conclusion, I recognize that this research would not have been possible without the financial assistance of Petróleo Brasileiro (PETROBRAS[2]), the Coordination for the Improvement of Higher Education Personnel (CAPES[3]) , the Federal University of Uberlândia and the Department of Mechanical Engineering, and express my gratitude to those agencies.

[1] MFLAB:<http://mflab.mecanica.ufu.br>
[2] PETROBRAS <http://www.petrobras.com.br/>
[3] CAPES <http://www.capes.gov.br/>

"Das Böse existiert nicht,
genauso wenig wie die Kälte und die Dunkelheit.
Gott hat das Böse nicht geschaffen.
Sondern es ist das Ergebnis dessen,
was Gottes Herz noch nicht berührt hat."

"Evil does not exist,
It is just like darkness and cold,
God did not create evil.
Evil is the result of what happens
when man does not have God's love present in his heart."

Albert Einstein - (1879 - 1955)

Abstract

Erosive wear is usually a decisive factor for failure of pipelines plants. Many industrial processes which require conveying of erosive particles are directly exposed to problems of leakage or contamination. As a result, unnecessary costs are needed by maintenance operations. This industrial concern is responsible for leading researchers to develop analysis tools which can precisely quantify the problem of erosion. Due to this fact, to validate the CFD model, numerical results for the standard elbow are compared to the experimental data. After that, a vortex chamber was added to the standard elbow, preserving the same geometry characteristics (*e.g.*, diameter and curvature radius) as well as the simulation parameters (*e.g.*, initial velocity, density, viscosity, etc.). Based on four-way-coupled simulations of the gas-solid flow in both geometries, the comparison between the standard and vortex-chamber elbow results was performed and a detailed analysis of the mass loading influence on the flow and on the penetration rate was reached. The present work used the finite-volume, unstructured code UNSCYFL3D, which solves the gas flow using the fully coupled Euler-Lagrange approach. The two-layer k-epsilon was used to model turbulence effects. Interestingly, the results show that the penetration ratio in the vortex-chamber elbow does not exponentially reduces with the increase of the mass loading, distinguishing from the behavior observed in standard elbow. Another important finding is that the addition of the vortex chamber significantly shows the efficiency of the cushioning effect. Comparing the peak of penetration ratio in both elbow designs for a mass loading of 1.0, the reduction was around 93% when the vortex chamber is present. Therewith, based on numerical analyses of the coupled gas-solid flow the physical mechanism for the cushioning effect is proposed.

Key-words: Elbow Erosion, Vortex-chamber Elbow Erosion, Mass Loading, Four-Way Coupling, Inter-Particle Collisions, Cushioning Effect.

Resumo

O desgaste erosivo é geralmente um fator decisivo na ruptura de gasodutos. Muitos processos industriais que necessitam transportar partículas erosivas estão diretamente expostos a problemas de vazamento ou de contaminação. Como resultado, custos desnecessários são usados em operações de manutenção. Essa preocupação industrial é responsável por motivar os pesquisadores a desenvolver ferramentas de análise que possam quantificar com precisão o problema da erosão. Devido a esse fato, para validar o modelo de CFD, os resultados numéricos para o cotovelo padrão são comparados com dados experimentais. Depois disso, uma câmara de vórtice foi adicionada ao cotovelo padrão, mantendo as mesmas características geométricas (*e.g.*, diâmetro e raio de curvatura), bem como os parâmetros de simulação (*e.g.*, velocidade inicial, densidade, viscosidade, etc.). Com base em simulações com quatro vias de acoplamento do escoamento gás-sólido em ambas geometrias, a comparação entre os resultados de cotovelo padrão e do cotovelo com câmara de vórtice foi realizada e uma análise detalhada da influência da carga mássica no escoamento e na taxa de penetração foi obtida. O presente trabalho utilizou o código de volumes finitos UNSCYFL3D, que resolve o escoamento de gás usando a abordagem de Euler-Lagrange totalmente acoplada. O modelo k-epsilon duas camadas foi usado para modelar os efeitos de turbulência. Curiosamente, os resultados mostram que a taxa de penetração no cotovelo com câmara de vórtice não reduz exponencialmente com o aumento da carga mássica, contradizendo o comportamento observado no cotovelo padrão. Outra descoberta importante é que a adição da câmara de vórtice mostra significativamente a eficiência do efeito de amortecimento. Comparando-se o pico da taxa de penetração em ambos os modelos de cotovelo para uma carga mássica de 1.0, a redução foi cerca de 93 % quando a câmara de vórtice está presente. Com base em análises numéricas do escoamento de gás-sólido acoplado, o mecanismo físico do efeito de amortecimento é proposto.

Palavras-chaves: Erosão em Cotovelos, Erosão em Cotovelos com Câmara de Vórtice, Carga Mássica, Quatro-Vias de Acoplamento, Colisões entre Partículas, Efeito de Amortecimento.

List of Figures

List of Tables

List of abbreviations and acronyms

CFD	Computational Fluid Dynamics
DES	Detached Eddy Simulation
DNS	Direct Numerical Simulation
FVM	Finite Volume Method
LES	Large Eddy Simulation
MFlab	Laboratory of Fluid Mechanics
NSE	Navier Stokes Equation
NPS	Nominal Pipe Size
PETROBRAS	Petróleo Brasileiro
RANS	Reynolds-Averaged Navier–Stokes equations
RMS	Root Mean Square
SIMPLE	Semi-Implicit Method for Pressure-Linked Equations
TKE	Turbulence Kinetic Energy

List of symbols

δ_{ij}	Kronecker delta
g_i	Gravity component

Contents

1 Introduction

Particles carried by a fluid flow is a common situation in many engineering systems. The necessity to model and predict detailed information about these kind of flows became a persistent issue in the study of multiphase flows over the past few decades. By understanding the dynamics of motion, it is possible to make improvements and increase the safety during the operation of these systems.

Throughout the 60's a new theoretical approach has been developed, the Computational Fluid Dynamics (CFD). The Computational Fluid Dynamics aims to simulate flow through numerical methodologies designed to represent a physical phenomenon. Although its development begun over 50 years ago, only in the 90's it started to have greater acceptance in the industry, especially in aeronautical projects. Nowadays, the Computational Fluid Dynamics has become an important tool to study flow problems, helping designers to optimize single and multiphase systems. In wear-related problems, the CFD is used as a tool for predicting the wear in various environments and due to its complexity unfeasible the use of empirical correlations.

In this context, many conveying systems are constantly exposed to abrasive wear issues. The most common mechanism responsible for this kind of surface damage is classified as erosive wear. In many industrial processes, this type of wear arises from the impingement of solid particles against the surface and have noticeable consequences on equipment reliability and safety. The abrasive wear can be a problem in cyclones separators, propellers and pumps (*cf.* Fig. 1), but in pneumatic conveying systems erosive wear can be even more serious (MILLS, 2004).

Figure 1 – Example of erosive wear in a pump casing.

Source: <http://goo.gl/uQfBFd>

Generally speaking, erosive wear is a problem which industry has learned to live. Although there are many ways to reduce the magnitude of the problem, relate the conveyed material and the system itself requires a large number of variables to be taken into account. In addition, maintenance time and operating costs are also important factors that lead companies to decide which is the best method for the reduction of erosion in their equipment. For an entire pipeline plant, the effects of different elements (*e.g.*, constrictions, pipe shapes and pipe fittings) have to be considered. Due to the nature of the transport process, piping systems are willing to wear when abrasive particles have to be conveyed. When particles are carried in suspension through the air, high conveying air velocities are required to keep the material moving, in order to prevent pipeline obstruction. In this context, pipe fittings provide pneumatic conveying systems with their flexibility in change the flow direction, however, these spots become more susceptible to repeatedly collisions and rapid wear can occur.

The goal of this dissertation is to support oil and gas industry by analyzing the mechanisms responsible for the erosion reduction in elbows promoted by a vortex chamber. In agreement with both Petróleo Brasileiro (PETROBRAS) as well as the supervisor from the university, and supported by the acquired knowledge during the literature review, it was decided to focus the research on the erosion reduction with the increase of the mass loading for both standard and vortex-chamber elbows.

The present dissertation is organized as follows: Chapter 2 discusses the objective and the method to reach it. In chapter 3, the background theory is presented as well as an overview of the elbows studied. Chapter 4 presents an overview of the relevant equations for gas/particle phase and erosion prediction. Chapters 5 and 6 describes the type of discretization and the particle phase algorithm, respectively. Chapter 7 presents a summary of the experiments and the numerical approach applied.The dissertation is concluded in Chapter 9 and future research recommendation are given in Chapter 10.

2 Dissertation scope

After an exhaustive literature review, for a successful and fulfillment of the graduation research, it is of extreme importance to define the goal and a method to reach it. Both are elaborate in this chapter. First Section 2.1 presents the research objective, after which a few words are spend on the relevance of the project in Section 2.2. Finally, in Section 2.3, a methodology is presented in order to reach the objective.

2.1 Research objective

There are two factors that directly influenced the definitive research objective of the current dissertation. Besides the literature acquired during the literature research, the suggestions and advices from the university supervisor are taken into account. PETROBRAS project suggestions are focused on solve problems related to wear in oil and gas industry, whereas my supervisor also draw attention to the scientific value of the research. For this reason, the research objective is divided into a primary and secondary objective.

The first objective relates to the research from a scientific perspective. This objective forms the basis to complete the research.

Carry out an investigation of the mass loading effects on the erosion of a ninety-degree-elbow, by simulating the elbow with an in-house CFD code.

The reason for focusing on the ninety-degree-elbow is related to validate the erosion prediction model with experiments, implement it in the code and analyze its capacity to deal with a variety of erosion problems in engineering with sufficient accuracy.

The second objective covers the part of the research that is of particular interest for PETROBRAS.

Predict the erosion profile in a vortex-chamber elbow for different mass loadings, aiming to verify its benefits when compared with the standard elbow geometry.

The reduction of erosion in cyclones separators and conveying systems are of particular interest for the company. For engineering purpose they require to know the magnitude of erosion acting on the equipment surface and the effects of the mass loading on the erosive process.

Both objectives are fulfilled simultaneously throughout this dissertation, whereas the conclusions can be found in Chapter 9.

2.2 Relevance

For this research, the only available simulation tool is CFD. Unfortunately erosion experimenting and measuring are not feasible. During the literature survey no example of solely the application of CFD onto a vortex-chamber elbow was found. Hence it would be rather novel to produce useful results using solely CFD. The standard elbow validation process will form one of the key parts in successfully acquiring these results. So besides the benefits for PETROBRAS, the research will also contribute to the scientific community.

2.3 Methodology

Knowing the research objectives it is possible to outline an initial methodology. This process is devised with the knowledge obtained during the literature review. It is schematically showed in Fig. 2 by placing the various steps in blocks and connecting them via arrows.

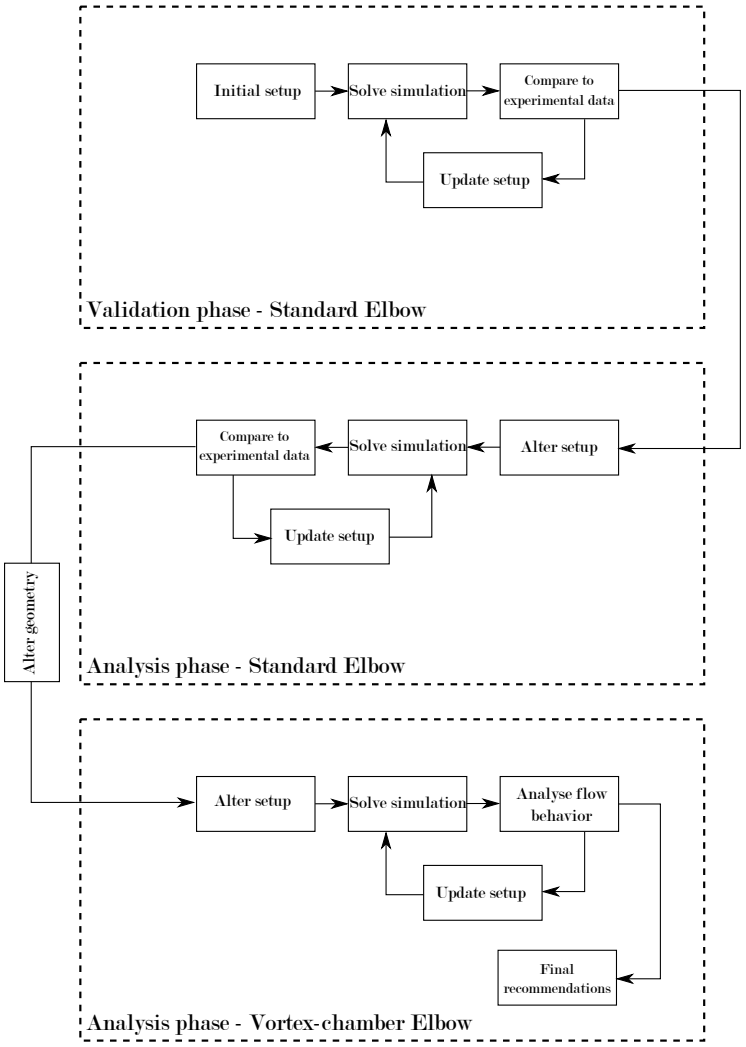

Figure 2 – Methodology used to reach the research objective.

Two phases can be distinguished; a validation phase and an analysis phase. The goal of the validation phase is to come up with a simulation setup that provides sufficiently accurate results in order to be used for the standard elbow simulations. In the analysis phase, both standard and vortex-chamber elbows are simulated for different values of mass loadings. The next lines explain both phases in details.

Validation phase

For the standard elbow an initial simulation setup is created based on literature and different erosion prediction models are tested. After find the best model, the simulation is ran and the resulting erosion profile is compared to existing experimental data. Depending on the outcome, the setup is updated in order to match both data sets more closely. Note that the updates are based on acquired literature and preserves the experimental characteristics. The complete validation phase is covered in Section 8.1.1 of this report.

Analysis phase

Once the simulation shows good agreement with the experimental data, the setup is altered such that it solves the flow and the erosion for different mass loadings. The resulting simulations can provide important insight into the changes of the erosion profile due to the mass loading variations. After this stage, the vortex-chamber geometry is created and the validate standard elbow simulation setup serves as an initial setup for the vortex-chamber simulations.

Finally, the vortex-chamber elbow is simulated with various mass loadings while using the best known simulation setup employed for the standard elbow. By analyzing the resulting dataset, it becomes possible to obtain remarkable results on both elbows simulations. The complete analysis phase is covered in Sections 8.1 and 8.2 of this report.

However before elaborating the research objective, first some background theory is required. This should provide the reader with a basic understanding of erosion wear and numerical techniques to compute them. The following set of chapters, bundled in Chapters 3 to 6, presents this theory.

3 Background theory

Several characteristics make the erosion profile inside pipelines and elbows significantly different. Hence the Computational Fluid Dynamical (CFD) techniques required to simulated the flow differ as well. This part of the dissertation will present the background theory required to understand the basic erosion phenomena occurring inside pipes and the CFD techniques employed to simulate them.

3.1 Types of wear

As described in many books, (*e.g.*, Gahr (1987) and Hutchings (1992)), different types of wear may be separated by referring to the basic material removal mechanisms, the wear mechanisms, that cause the wear on a microscopic level. There are many attempts to classify wear by wear mechanisms, but a commonly accepted first order classification distinguishes between *adhesive wear*, *abrasive wear*, *wear caused by surface fatigue*, and *wear due to tribochemical reactions*.

Very commonly, the damage observed on a tribologically loaded surface is a result of two or more coexisting or interacting surface damage types. Interacting damage types may lead to unproportionally high wear rates, as for example in oxidation-enhanced surface cracking; adhesive wear may however also be suppressed by oxidation (ASKELAND; FULAY; WRIGHT, 2010).

In this context, the present dissertation will exclusively focus on the erosion due to particles. It is known that other types of wear can coexist, however, carry out a study with more than one type of wear at the same time can significantly increase the difficulty to find accurate mathematical models. Due to this fact, all the geometries studied in this report as well as the experimental database have their surface damaged preferentially by erosion, avoiding the interference of other types of wear and facilitating an accurate analysis of the models used in the simulations.

3.1.1 Erosion due to particles

Erosion is defined as the wear resulted by the interaction between a solid surface and a fluid flow containing abrasive particles with a certain speed, or the impact of free moving liquid (or solid) particles on a solid surface (FINNIE, 1960). We can divide the understanding of erosion in two major parts, the first being the determination of the fluid flow conditions of the number, direction, and velocity of the particles striking the surface. The second part may be defined as the calculation of surface material removed,

with the data acquired from the first part. Clearly, the first part of the erosion process is characterized as a fluid mechanics problem, with the fluid flow transporting the particles into the surface, which defines the erosion wear (PEREIRA; SOUZA; MORO, 2014).

Erosion wear is dependent of the number of particles striking a surface, as well as the physical quantities associated with it, such as particle velocity and their direction relative to the surface to be struck. It is known that these quantities are noticeably determined by the flow conditions. In other words, any minor change in the flow conditions such as viscous regime or temperature might bring large variations in the erosion rate. For example, in operations where the flow direction changes quickly such as turbine blade erosion is usually more severe than in a straight run of piping. Other erosion-increasing factor is the local turbulence generated from roughened surface or misaligned parts (FINNIE, 1960).

3.1.2 Erosion mechanisms

According to the literature, there are several ways to describe the mechanism of erosion, as provided from different authors. Therefore, it is difficult to establish only one mechanism as the most reliable and real mechanism. The most used in the literature are the ones proposed by Finnie (1960) and Hutchings (1992).

Finnie (1960) proposed a mechanism of erosion in which the particle acts as a miniature machine tool in which the surface material is cut, generating a chip. Also, for the erosion of ductile metals, at oblique impact, this mechanism happens irrespective of its shape and size.

Hutchings (1992) proposed a similar mechanism. However, he split the cutting action into three different types, relying on the shape and the orientation of the eroding particle. The first type occurs when there is erosion by oblique impact of spherical particles, and the material is removed by a plowing action, moving materials to the front and side of the particle. The second and third types occur when there is the collision of angular shaped particles, and they differ from each other in the orientation of the erodent particle as it strikes the target surface, as well as the direction of the particle during the contact with the surface; in other words, if the particle rolls forward or backward during contact. Type I cutting is defined when the particle rolls forward during the contact, and material is removed by repeated impacts on a prominent lip formed by the indenting angular particle. Type II cutting is defined when the particle rolls backward, and the material is removed as if the erosion was a machining operation, with the material being removed as a chip due to the fact that there's a sharp tip of the erodent particle, working as a machining tool (HUTCHINGS, 1992).

3.1.3 Influence of the flow in the erosion

Figure 3 shows four flow configurations commonly found in engineering applications. The first configuration illustrates an impinging jet, which covers a wide range of applications, representing from research configurations to abrasion machining; Figure 3b shows the flow configuration found in flows over turbine blades and turbo machinery; Figure 3c shows the flow configuration that occurs in pneumatic transport of solids and in piping; Figure 3d represents the flow configuration found in heat transfer devices (HUMPHREY, 1990).

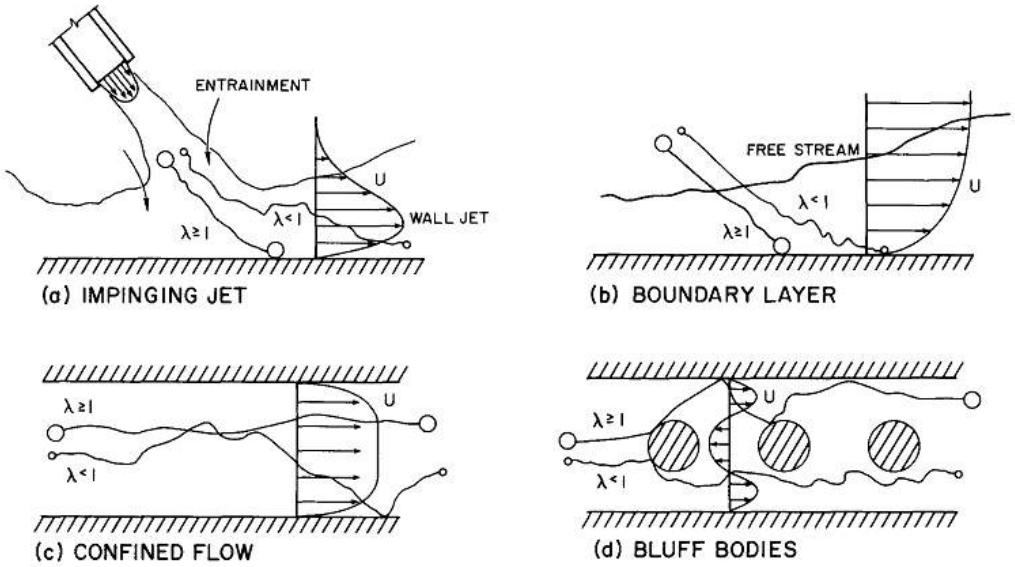

Figure 3 – Examples of flow configurations related to erosion due to impact by solid particles (HUMPHREY, 1990).

The dynamic behavior of large and small particles is interpreted briefly in Fig. 1. The ability of a particle to respond to changes imposed by the flow, and therefore, change its trajectory is characterized by the number λ, which is defined by the ratio of two time scales that characterizes the dynamics of both solid and fluid phases, respectively. In Fig. 1, this number simply represents the particle dimension; for $\lambda >> 1$, particles have high momentum and respond slowly to flow changes; on the other hand, for $\lambda << 1$, particles tend to follow the flow, being an alternative to flow visualization. This is analogous to the Stokes number, classically used in particulate systems research.

The incident velocity magnitude of a particle depends on its interaction with the fluid, with other particles, and with the wall. The behavior of these interactions depends of the flow viscous regime (laminar or turbulent), as well as the size, shape and density of particles. Interactions between particles are strongly related to the local particle concentration, potentially causing low or high concentration regions (PEREIRA; SOUZA; MORO, 2014).

3.2 Pipe fittings

A fitting is used in pipe plumbing systems to connect straight pipe or tubing sections, to adapt to different sizes or shapes, and for other purposes, such as regulating or measuring fluid flow. Some examples of pipe fittings are showed in Fig. 4. The term plumbing is generally used to describe conveyance of water, gas, or liquid waste in ordinary domestic or commercial environments, whereas piping is often used to describe high-performance (*e.g.*, high pressure, high flow, high temperature, hazardous materials) conveyance of fluids in specialized applications (PARISHER; RHEA, 2002). Pipe fittings are commonly used in flow systems and can strongly influence flow (DESHPANDE; BARIGOU, 2001).

Although there is a plenty of pipe fittings, the focus of this work will be aimed only for two types of elbows: the standard elbow and the vortex-chamber elbow. This elbows are discussed in the next two sections, respectively.

Figure 4 – Examples of pipe fittings.

Source: <http://goo.gl/Sl97VE>

3.2.1 Standard elbow

An elbow is a pipe fitting installed between two lengths of pipe or tubing to allow a change of direction, usually a 90° or 45° angle. A 90 degree elbow (Fig. 5) is also called a "90 bend" or "90 ell" but in this report the name ”standard elbow” is used in order to facilitate the treatment between the two types studied. It is a fitting which is bent in such a way to produce 90 degree change in the direction of flow in the pipe. It is used to change the direction in piping and is also sometimes called a "quarter bend" (MILLS, 2004). A 90 degree elbow attaches readily to plastic, copper, cast iron, steel and lead. It can also

attach to rubber with stainless steel clamps. It is available in many materials like silicone, rubber compounds, galvanized steel, aluminum, etc. The main application of a standard elbow is to connect hoses to valves, water pressure pumps, and deck drains.

Figure 5 – Example of a 90 degree elbow.

Source: <http://goo.gl/UznH03>

Most elbows are available in short radius or long radius variants. The short radius elbows have a center-to-end distance equal to the Nominal Pipe Size (NPS) in inches, while the long radius is 1.5 times the NPS in inches. Short elbows are widely available, and are typically used in pressurized systems. Long elbows are typically used in low-pressure gravity-fed systems and other applications where low turbulence and minimum deposition of entrained solids are of concern.

Elbows are often used in oil and gas production systems, and they cause redistribution of gas and liquid which can affect distribution of corrosion inhibitors within and downstream of the bends. Elbows are also a location susceptible to the impact of particles along the outer radius (VIEIRA et al., 2014).

3.2.2 Vortex-chamber elbow

In 1983, HammerTek Corporation proposed a variation of the standard elbow design (PAULSON; HESS, 1983) which will be named along this paper as vortex-chamber elbow (Fig. 6). Is also called a ”Vortice Ell” or ”Smart Elbow” and allows very compact changes of direction (either 90° or 45°) within pneumatic conveying pipe systems, eliminating or greatly reducing wear in both the bend and/or secondary wear in the straight section immediately after the bend.

The unique feature of the vortex-chamber elbow is the circular chamber positioned on the heel, called the vortex chamber. This chamber creates a non-impact deflection zone which guides the conveyed product smoothly round the elbow. As well as eliminating or greatly reducing wear, this feature also creates laminar flow at the exit of the elbow (ROTA, 2001).

Figure 6 – Example of a vortex-chamber elbow.

Source: <http://goo.gl/q26dxh>

Although not commonly found in daily life, will be shown during this work that for industrial applications which require the transport of abrasive particles the vortex-chamber elbow provides an excellent alternative to the standard elbow.

3.3 CFD applied to erosion problems

Many efforts have motivated the research community to understand the physics behind the erosion process in pipe systems. Experimental investigations (CHEN; MCLAURY; SHIRAZI, 2006; CHEN; MCLAURY; SHIRAZI, 2004; VIEIRA et al., 2014; TAKAHASHI et al., 2010; MAZUMDER; SHIRAZI; MCLAURY, 2008) support the development of empirical correlations and models that are capable to predict the erosion behavior both single and multiphase flows (AHLERT, 1994; NEILSON; GILCHRIST, 1968; OKA; OKAMURA; YOSHIDA, 2005a; OKA; OKAMURA; YOSHIDA, 2005b; ZHANG et al., 2007). In this sense, progress in understanding the erosion due to particles has been achieved by the utilization of CFD models that can accurately simulate the fluid and particle motion through pipelines and bends (LAíN; SOMMERFELD, 2013).

Four empirical models for the calculation of the erosion ratio were tested in this work. It should be noticed that these models are implemented in Unsteady Cyclone Flow 3D (UNSCYFL3D), working alongside the fluid and particle models. These models are presented below but only the Oka, Okamura e Yoshida (2005a) model was used to simulate all the cases. Oka, Okamura e Yoshida (2005a) will be explained in details in Section 4.3.

3.3.1 Erosion correlations

The erosion rate is defined as the mass of removed material per unit of area per unit of time. It is calculated on the walls by accumulating the damage each particle causes

when colliding against the wall surface. It is given by:

$$E_f = \frac{1}{A_f} \sum_{\pi(f)} \dot{m}_\pi \, e_r \tag{3.1}$$

in which A_f is the face area, $\dot{m}_\pi$ is the particle mass flow rate represented by each computational particle that collides with the face and e_r is the erosion ratio, which consists in the ratio of mass of eroded material over mass of erodent material and must be computed by a correlation.

The erosion is formulated in terms of the penetration ratio, accordingly to the expression:

$$\text{Penetration Ratio} = \frac{E_f}{\dot{m}_p \, \rho} \tag{3.2}$$

where $\dot{m}_p$ is the inlet sand mass flow rate (kg/s) and ρ is the elbow material density (kg/m^3). The penetration ratio represents the thickness of material removed from the wall over the mass of sand injected into the elbow.

The correlation proposed by Ahlert (1994) is:

$$e_r = K F_s f(\alpha) \left(\frac{u_p}{u_{ref}} \right)^n \tag{3.3}$$

in which K is a material-dependent constant, whose value was assigned 2.388×10^{-7} in this work, F_s is a factor to account for the shape of the particles, $f(\alpha)$ is a function expressing the dependency on the particle incidence angle, u_{ref} is a constant reference velocity and n a constant exponent. The shape coefficient F_s is reported to take the value 1.0 for angular particles, 0.53 for semi-rounded particles and 0.2 for fully rounded particles.

The angle function $f(\alpha)$ is split into two ranges. Below the user specified transition angle α_0 is a polynomial in, the incidence angle in radians. Above the transition angle, $f(\alpha)$ follows a trigonometric relationship,

$$f(\alpha) = x \cos^2(\alpha) \sin(w\alpha) + y \sin^2(\alpha) + z \tag{3.4}$$

The constants w, x and y are 1.0, 0.147 and -0.745 respectively, whereas z is calculated internally by requiring that $f(\alpha)$ is continuous at α_0.

The correlation proposed by Neilson e Gilchrist (1968) is:

$$e_r = e_{rC} + e_{rD} \tag{3.5}$$

in which e_{rC} and e_{rD} represent contributions from cutting and deformation respectively. The cutting erosion is modeled as a function of the incidence angle α.

$$\begin{aligned} e_{rC} &= \frac{u_p^2 \cos^2(\alpha) \sin\left(\frac{\pi\alpha}{2\alpha_0}\right)}{2\varepsilon_C} \text{ if } \alpha < \alpha_0 \\ e_{rC} &= \frac{u_p^2 \cos^2(\alpha)}{2\varepsilon_C} \text{ if } \alpha > \alpha_0 \end{aligned} \tag{3.6}$$

with α_0 being the transition angle, normally set as 45°, and ε_C the cutting coefficient, specified as 3.332×10^7. Similarly, the deformation erosion is given by,

$$e_{rD} = \frac{\max(u_p \sin(\alpha) - K, 0)^2}{2\varepsilon_D} \tag{3.7}$$

where ε_D is the deformation coefficient, set as 7.742×10^7, and K the cut-off velocity, below which no deformation erosion occurs. In this work, the cut-off velocity was set to zero.

The correlation proposed by Zhang et al. (2007) is:

$$e_r = C(BH)^{-0.59} F_s V_p^n F(\alpha) \tag{3.8}$$

$$F(\alpha) = 5.4\alpha - 10.11\alpha^2 + 10.93\alpha^3 - 6.33\alpha^4 + 1.42\alpha^5 \tag{3.9}$$

where C and n are empirical constants, equal to 2.17×10^7 and 2.41, respectively. BH is Brinnell hardness of the eroded material, F_s is the particle shape coefficient, in this case 0.2 for perfectly round particles, V_p is the particle impact velocity and α is the particle incidence angle.

3.3.2 Coefficients of restitution

In order to obtain an accurate prediction of the particle trajectories, it is necessary to select a particle restitution model. Conversely, knowledge on how particles behave after collisions with walls is needed. Upon collision, the particle loses energy, and the rebound velocity is lower than the particle incident velocity. This effect is taken into account through the coefficients of restitution. In this work, three different models were used, all of them being derived from experimental studies.

The model proposed by Forder, Thew e Harrison (1998) for the normal and parallel coefficients of restitution is given, respectively, by:

$$e = 0.988 - 0.78\alpha + 0.19\alpha^2 - 0.024\alpha^3 + 0.0027\alpha^4 \tag{3.10}$$

$$e_{par} = 1 - 0.78\alpha + 0.84\alpha^2 - 0.21\alpha^3 + 0.028\alpha^4 - 0.022\alpha^5 \tag{3.11}$$

where α is the particle incidence angle in radians.

Sommerfeld e Huber (1999) proposed a model for the normal coefficient of restitution only, regarding the parallel component equal to one. The reason for that is the low contribution of the parallel component on the reflection of particles after collision. The correlation for the normal restitution coefficient is given by:

$$e = \max(1 - 0.013\alpha, 0.7) \tag{3.12}$$

Despite the coefficients presented above the model proposed by Grant e Tabakoff (1975), which was not shown here, has a better accuracy due to its relation on experimental data on aluminum and sand. This model will also be presented in Section 4.3.

3.3.3 Coefficients of friction

Friction is not itself a fundamental force but arises from forces between the two contacting surfaces. The complexity of these interactions makes the calculation of friction from first principles impractical and necessitates the use of empirical methods for analysis and the development of theory.

An empirical model proposed by Sommerfeld e Huber (1999) described below:

$$\mu = \max(0.5 - 0.175\alpha, 0.15) \tag{3.13}$$

It is worth noticing that the static and dynamic coefficients of friction were assumed to be equal in this work. No considerable difference was detected by prescribing the dynamic coefficient lower than the static one.

4 Mathematical models

It is clear that many different simulations techniques are available for the present study. However not every technique is suitable for the type of flow being solved. Based on the type of flow, assumptions can be made that simplify the flow equations. This leads to a set of equations that should resolve the flow field with sufficient accuracy while using the computational resources as effective as possible.

This chapter presents the mathematical models that should be sufficient for the current study. For the gas phase solution the RANS method with a two-layer k-epsilon turbulence model is employed. The particulate phase is treated in a Lagrangian framework, having the equation of motion based on Newton's second law. For the erosion calculation the most accurate model is proposed and utilized. Every technique and model will be detailed separately.

The chapter is structured as follows. First, Section 4.1 presents the flow equations. Then, Section 4.2 shows the particle motion equations. Finally, the employed erosion model is presented in Section 4.3.

4.1 Gas phase equations

Simulations of fluids are based on the Navier Stokes Equations (NSE). In tensor notation the continuity and Cauchy momentum equation are respectively,

$$\frac{\partial \rho}{\partial t} + \frac{\partial (\rho u_i)}{\partial x_i} = 0 \tag{4.1}$$

$$\frac{\partial (\rho u_i)}{\partial t} + \frac{\partial (\rho u_i u_j)}{\partial x_j} = -\frac{\partial p}{\partial x_i} + \frac{\partial \tau_{ij}}{\partial x_j} + f_i \tag{4.2}$$

where p is the pressure, ρ is the fluid density, u_i represents the i component of the velocity vector, τ_{ij} denotes the molecular viscous tensor and f_i is the component i of the source term.

For a Newtonian fluid, where ν represents the the kinematic viscosity of the fluid, the tensor is modeled with the Stokes model of viscous stress,

$$\tau_{ij} = \nu \left(\frac{\partial u_i}{\partial x_j} + \frac{\partial u_j}{\partial x_i} \right) - \frac{2}{3} \mu \delta_{ij} \tag{4.3}$$

For the present study, a steady-state and incompressible flow is assumed. External forces such as gravity forces and source terms due to phase interaction (Su_{ip}) are added to the momentum equation. Now the NSE for continuity and momentum are,

$$\frac{\partial(\rho u_i)}{\partial x_i} = 0 \tag{4.4}$$

$$\frac{\partial(\rho u_i u_j)}{\partial x_j} = -\frac{\partial p}{\partial x_i} + \frac{\partial}{\partial x_j}\left[\nu\left(\frac{\partial u_i}{\partial x_j} + \frac{\partial u_j}{\partial x_i}\right)\right] + Su_{ip} + \rho g_i \tag{4.5}$$

The above presented set of equations allows the flow to experience turbulent behavior. Hence the flow contains turbulent kinetic energy (E) that is distributed over eddies with varying sizes. When all the turbulence is resolved, the mesh should be fine enough to capture even the smallest eddies. This technique is called Direct Numerical Simulation (DNS). However with the current available hardware this is only possible with very simple geometries and low Reynolds number flows. In order to get a clearer view of which eddies are resolved using various methods, a logarithmic plot of this energy with respect to the reciprocal of the Eddy size, the wavenumber (k), is given in Fig. 7.

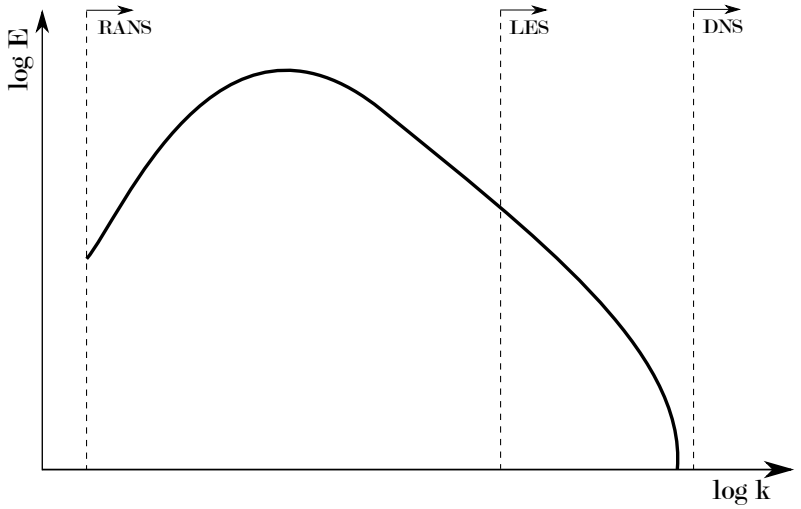

Figure 7 – The turbulent kinetic energy distributed over eddies of different sizes (FRöHLICH; TERZI, 2008).

From this figure it can be seen that DNS resolves all the turbulent kinetic length scales and thus all the turbulence. On the other hand RANS simulations model all the turbulence and thus non of the eddies are resolved. It can be seen that most of the kinetic energy is located in the large eddies. Large Eddy Simulation (LES) is based on this fact and resolves the large scales while the small scales are approximated using mathematical models. In some regions of a flow field, like the boundary layer, the large eddies become very small as well, requiring very small cell sizes.

For the current study, a confined flow is considered. Since high Reynolds number is present and complex flow phenomena occur, DNS is not an option for solving the flow. LES is also discarded as an option due to its high computational costs. Since RANS uses the least computational resources while still providing sufficiently accurate results, the main focus lies on this technique. The next section shows more detail about this method.

4.1.1 Reynolds Averaged Navier Stokes simulations

Reynolds (1895) derived a statistical approach to approximate the Navier Stokes Equations. By time averaging the equations, only the mean properties of the flow remain. According to Reynolds, for most turbulent flows only these averages characteristics are of interest. The quantities present in the NSE are split into a mean and a fluctuating component. For the velocity this yields in tensor notation the following,

$$u_i(\vec{x}_i, t) = \overline{u}_i(x_i) + u_i^{'}(x_i, t) \tag{4.6}$$

for which holds that,

$$\overline{u^{'}}_i(x_i, t) = 0 \tag{4.7}$$

Replacing all time varying quantities in the simplified NSE, as derived in the previous section, with this definition and rearranging the terms yields for the continuity and momentum equation in tensor notation,

$$\frac{\partial \overline{u_i}}{\partial x_i} = 0 \tag{4.8}$$

$$\frac{\partial(\overline{u_i}\,\overline{u_j})}{\partial x_j} = -\frac{1}{\rho}\frac{\partial \overline{p}}{\partial x_i} + \frac{\partial}{\partial x_j}\left[\nu\left(\frac{\partial \overline{u_i}}{\partial x_j} + \frac{\partial \overline{u_j}}{\partial x_i}\right) - \overline{u_i^{'} u_j^{'}}\right] \tag{4.9}$$

From the equations above it can be seen that for three-dimensional flow, four equations and ten unknowns are present. Besides three unknown velocity components and the pressure, the later equation contains an additional six unknowns. These are included in the Reynolds stress tensor,

$$\overline{\overline{\tau_{ij}}} = -\overline{u_i^{'} u_j^{'}} \tag{4.10}$$

The Reynolds stress tensor has to be modeled in order to solve the RANS equations, which is also known as turbulence modeling. The quality of solution depends largely on the quality of the applied turbulence model. Section 4.1.2 describes the model employed for the current research.

4.1.2 Turbulence model

The Reynolds stress tensor, $\overline{\overline{\tau_{ij}}}$, is often approximated by the Boussinesq (1877) hypothesis in order to link the Reynolds stresses with the mean velocity gradients. This approximation is formulated as follows,

$$\overline{\overline{\tau_{ij}}} = -\nu_t \left(\frac{\partial \overline{u}_i}{\partial x_j} + \frac{\partial \overline{u}_j}{\partial x_i} \right) + \frac{2}{3} k \delta_{ij} \tag{4.11}$$

In this equation both the kinematic Eddy viscosity, ν_t and the turbulent kinetic energy, k, are unknown. Closure models provide a means to compute these extra quantities by introducing extra equations. The models can be classified into four different types; algebraic models, one equation models, two equation models and second order closure models. Thereof, according to Wilcox (1994), for RANS simulations the two equation models are the most popular. On the other hand, when a Detached Eddy Simulation (DES) simulation is performed, often a one equation model is employed. The term one or two equation turbulence model implies that one or two extra transport variables are used for the formulation that are related to ν_t and k.

For RANS simulations the best choice is to use the $k - \epsilon$ or the $k - \omega$ turbulence model. These models solve two extra transport equations. One for k and one for ϵ or ω. These extra variables relate to ν_t for the $k - \epsilon$ model as,

$$\nu_t = C_\mu \frac{k^2}{\epsilon} \tag{4.12}$$

and for $k - \omega$ as,

$$\nu_t = \frac{k}{\omega} \tag{4.13}$$

For this dissertation, a variation of the $k - \epsilon$ is used and will be discussed in details in the following subsections.

4.1.2.1 Two layer $k - \epsilon$ model

The most famous model of the two is the $k - \epsilon$ model of which the standard is set by Jones e Launder (1972). In this formulation the second transport variable used is the turbulent kinetic energy dissipation ϵ. In literature the method is often referred to as the Standard $k - \epsilon$ model. When applying the Standard $k - \epsilon$ model, usually the closure coefficients published in Launder e Sharma (1974) are used.

The two layer $k - \epsilon$ model is employed, as it can handle well both the core flow and the near wall region. Essentially, it consists in solving the standard model for the turbulent flow region and a one equation model for the region affected by the viscosity. In

the one equation $k-\epsilon$ model, the conservation equation for k is retained, whereas ϵ is computed from,

$$\epsilon = \frac{k^{3/2}}{l_\epsilon} \tag{4.14}$$

The length scale that appears in Eq. (4.14) is computed from,

$$l_\epsilon = y\, C_l\, (1 - e^{-Re_y/A_\epsilon}) \tag{4.15}$$

In Eq. (4.15), Re_y is the turbulent Reynolds number, defined as:

$$Re_y = \frac{\rho\, y\sqrt{k}}{\mu} \tag{4.16}$$

where y is the distance from the wall to the element centers. This number is the demarcation of the two regions, fully turbulent if $Re_y > Re_y^*$, $Re_y^* = 200$ and viscosity-affected, $Re_y < 200$. For the one equation model, the turbulent viscosity is computed from,

$$\mu_{t,2layer} = \rho\, C_\mu\, l_\mu \sqrt{k} \tag{4.17}$$

The length scale in the equation above is computed as below:

$$l_\mu = y\, C_l\, (1 - e^{-Re_y/A_\mu}) \tag{4.18}$$

In UNSCYFL3D code, both the standard $k-\epsilon$ and the one equation model described above are solved over the whole domain, and the solutions for the turbulent viscosity and the turbulence kinetic energy dissipation rate provided by both models are smoothly blended,

$$\mu_t = \lambda_\epsilon\, \mu_{t,standard} + (1 - \lambda_\epsilon)\, \mu_{t,2layer} \tag{4.19}$$

A blending function, λ_ϵ, is defined in such a way that it is equal to unity far from walls and is zero very near walls. The blending function used here is,

$$\lambda_\epsilon = \frac{1}{2}\left[1 + \tanh\left(\frac{Re_y - Re_y^*}{A}\right)\right] \tag{4.20}$$

The constant A determines the width of the blending function,

$$A = \frac{0.20\, Re_y^*}{\operatorname{artanh}(0.98)} \tag{4.21}$$

The purpose of the blending function λ_ϵ is to prevent solution divergence when the solution from both the standard and the one-equation models do not match. The constants in the length scale formulas, Eqs. (4.15) and (4.18), are taken from:

$$C_l = 0.4187 C_\mu^{-3/4} \quad A_\mu = 70 \quad A_\epsilon = 2C_l \tag{4.22}$$

Since no wall-functions are used, it is very important to refine the grid so as to have $y+ < 1$ in the first element away from the wall and ensure accurate results for the fluid flow.

4.2 Particle motion equations

As mentioned in Section 4, the dispersed phase is treated in a Lagrangian framework, in which each particle is tracked through the domain and its equation of motion is based on Newton's second law. The trajectory, linear momentum and angular momentum equations for a rigid, spherical particle can be written, respectively,

$$\frac{dx_{pi}}{dt} = u_{pi} \tag{4.23}$$

$$m_p \frac{du_{pi}}{dt} = m_p \frac{3\rho C_D}{4\rho_p d_p}(u_i - u_{pi}) + F_{si} + F_{ri} + \left(1 - \frac{\rho}{\rho_p}\right) m_p g_i \tag{4.24}$$

$$I_p \frac{d\omega_{pi}}{dt} = T_i \tag{4.25}$$

In the above equations, $u_i = U_i + u_i^{'}$ are the components of the instantaneous fluid velocity. The average fluid velocity U_i is interpolated from the resolved flow field, whereas the fluctuating component $u_i^{'}$ is calculated according to the Langevin dispersion model proposed by Sommerfeld (2001). d_p is the particle diameter and $I_p = 0.1\, m_p\, d_p^2$ is the moment of inertia for a sphere. Unlike most commercial CFD codes, UNSCYFL3D solves for the particle rotation. This is particularly important when dealing with large particles, which frequently collide with walls.

The empirical correlation proposed by Schiller e Naumann (1935) is used to evaluate the drag coefficient past each particle:

$$\begin{gathered} C_D = 24\, Re_p^{-1}(1 + 0.15\, Re_p^{0.687}) \text{ if } Re_p < 1000 \\ C_D = 0.44 \text{ if } Re_p > 1000 \end{gathered} \tag{4.26}$$

In Eqs. (4.26), Re_p is the particle Reynolds number $Re_p = \rho\, d_p|\vec{u} - \vec{u}_p|/\mu$.

The calculation of the shear-induced lift force is based on the analytical result of Saffman (1965) and extended for higher particle Reynolds numbers according to Mei (1992):

$$\vec{F}_s = 1.615\, d_p\, Re_s^{1/2}\, C_{ls}[(\vec{u} - \vec{u}_p) \times \vec{\omega}] \tag{4.27}$$

$\vec{\omega}$ is the vorticity, $Re_s = \rho\, d_p^2\, |\vec{\omega}|/\mu$ is the particle Reynolds number of the shear flow and $C_{ls} = F_{ls}/F_{ls,Saff}$ represents the ratio of the extend lift force to the Saffman force:

$$\begin{gathered} C_{ls} = (1 - 0.3314\,\beta^{0.5})e^{-0.1Re_p} + 0.3314\,\beta^{0.5} \text{ if } Re_p < 40 \\ C_{ls} = 0.0524(\beta\, Re_p)^{0.5} \text{ if } Re_p > 40 \end{gathered} \tag{4.28}$$

β is a parameter $\beta = 0.5\, Re_s/Re_p$ which varies with $0.005 < \beta < 0.4$.

The rotation-induced lift is computed based on the relation given by Rubinow e Keller (1961), which was extended to account for the relative motion between particle and fluid:

$$\vec{F}_r = \frac{\pi}{8}\,\rho\, d_p^3 \frac{Re_p}{Re_r}\, C_{lr}\, \frac{[\vec{\Omega} \times (\vec{u} - \vec{u}_p)]}{|\vec{\Omega}|} \tag{4.29}$$

In Eq. (4.29), $\vec{\Omega} = 0.5\,\vec{\nabla} \times \vec{u} - \vec{\omega}_p$ and $Re_s = \rho\, d_p^2\, |\vec{\Omega}|/\mu$. The lift coefficient C_{lr} is obtained from the correlation proposed by Lun e Liu (1997):

$$\begin{gathered} C_{lr} = \frac{Re_r}{Re_p} \text{ if } Re_p < 1 \\ C_{lr} = \frac{Re_r}{Re_p}(0.178 + 0.822\, Re_p^{-0.522}) \text{ if } Re_p > 1 \end{gathered} \tag{4.30}$$

Also, the rotating particle experiences torque from the fluid flow. The correlation of Rubinow e Keller (1961) was extended to account for the relative motion between fluid and particle at higher Reynolds number:

$$\vec{T} = C_r\, \frac{\rho\, d_p^5}{64} |\vec{\Omega}|\, \vec{\Omega} \tag{4.31}$$

The coefficient of rotation, C_r, was obtained from the following correlation, derived from and the direct numerical simulations of Dennis, Singh e Ingham (1980):

$$C_r = \frac{64\pi}{Re_r} \text{ if } Re_r < 32$$
$$C_r = \frac{12.9}{\sqrt{Re_r}} + \frac{128.4}{Re_r} \text{ if } Re_r > 32 \tag{4.32}$$

Forces such as Basset and virtual mass have been neglected. This is a reasonable assumption since the particle material density is over 1000 times the gas density (CROWE et al., 1997; CROWE; MICHAELIDES; SCHWARZKOPF, 2005).

The extension of the Euler/Lagrange approach to unstructured meshes requires the use of accurate interpolation schemes, since in the above equations the continuous phase properties must be determined at the particle center. A few interpolation schemes have been tried out, and the best compromise between accuracy and cost was obtained with the Sheppard's scheme. Basically, the velocity and vorticity components at the particle position are calculated by weighing the neighboring element values with their inverse distances from their centers to the particle position. For integrating the ordinary differential equations (4.23), (4.24) and (4.25), the analytical scheme was used for the linear and angular velocities.

Upon a particle colliding with a wall, the new particle linear and angular velocities after rebound are calculated according to the following conservation equations (BREUER; ALLETTO; LANGFELDT, 2012):

Nonsliding collision:

$$\vec{u}_p^{\,+} = \vec{u}_p^{\,-} - (1 + e_{par})\,\frac{2}{7}\,\vec{u}_{pr}^{\,-} - (1 + e)\,(\vec{u}_p^{\,-} \cdot \vec{n})\,\vec{n} \tag{4.33}$$

$$\vec{\omega}_p^{\,+} = \vec{\omega}_p^{\,-} - \frac{10}{7}\frac{1 + e_{par}}{d_p}\,\vec{n} \times \vec{u}_{pr}^{\,-} \tag{4.34}$$

Sliding collision:

$$\vec{u}_p^{\,+} = \vec{u}_p^{\,-} - (1 + e)\,(\vec{u}_p^{\,-} \cdot \vec{n})\left[\mu_d\,\frac{\vec{u}_p^{\,-}}{|\vec{u}_p^{\,-}|} + \vec{n}\right] \tag{4.35}$$

$$\vec{\omega}_p^{\,+} = \vec{\omega}_p^{\,-} - \frac{5}{d_p}(1 + e)\,(\vec{u}_p^{\,-} \cdot \vec{n})\,\frac{\mu_d}{|\vec{u}_p^{\,-}|}\,\vec{n} \times \vec{u}_{pr}^{\,-} \tag{4.36}$$

In the above equations, the superscripts $-$ and $+$ denote values prior to and after the collision, respectively, e_{par} is the parallel restitution coefficient, e is the normal restitution coefficient and μ_d is the dynamic friction coefficient. $\vec{n}$ is the normal unit vector

pointing outwards of the element face being impacted. $\vec{u}_{rp}$ is the relative velocity at the contact point:

$$\vec{u}_{pr} = \vec{u}_p - (\vec{u}_p \cdot \vec{n})\,\vec{n} + \frac{d_p}{2}\,\omega_p \times \vec{n} \tag{4.37}$$

Inter-particle collisions are modeled with a stochastic, hard-sphere model. As described by Oesterle e Petitjean (1993) and Sommerfeld (2001), for each computational particle, a fictitious collision partner is generated, and the probability of a collision is checked based on an analogy with kinetic theory of gases. This in turn requires that the average and RMS linear and angular velocities, as well as the particle concentration in each control volume, be sampled and stored every Lagrangian calculation. Although demanding a lot of memory, the method is rather economical and effective, and avoids the use of a deterministic collision model, which is quite expensive computationally.

Numerous experimental studies have shown evidence that wall roughness is important in the particle behavior. Therefore, their influence must be included in the modeling. As demonstrated by Lain, Sommerfeld e Kussin (2002) and Benson, Tanaka e Eaton (2004), the wall roughness plays a vital role in the dispersion of particles in pneumatic transport systems. In order to account for such effects, we implemented the model proposed by Sommerfeld e Huber (1999), to represent the effects of surface asperities on the particle flow. In summary, the wall roughness is simulated by assuming that the effective impact angle $\alpha_{geometric}$ is composed of the geometric impact angle α geometric added to a stochastic contribution due to wall roughness.

$$\alpha = \alpha_{geometric} + \xi \cdot \Delta\gamma \tag{4.38}$$

This stochastic contribution is sampled from a Gaussian distribution with a standard deviation $\Delta\gamma$, which depends on the structure of wall roughness and particle size. Unfortunately, the value of $\Delta\gamma$ must be calibrated so as to provide the best agreement between the experimental and simulated pressure losses.

When a structured grid is used, it is simple to determine the element hosting the particle, as there exists a straightforward relationship between the element index and its physical location. Because an unstructured grid is used in this work, there is the need for a specific algorithm to locate the particle after its final position is calculated by the integration of Eq. (4.23). For that purpose, the particle-localization algorithm proposed by Haselbacher, Najjar e Ferry (2007) is used and will be detailed in Section 6.

4.3 Erosion prediction equation

After a exhaustive search in literature, the works from Pereira, Souza e Moro (2014) and Duarte, Souza e dos Santos (2015) showed that the combination of the models proposed by Oka, Okamura e Yoshida (2005b) for the erosion ratio and Grant e Tabakoff (1975) for the coefficient of restitution were the most suitable for the erosion prediction when ninety-degree-elbows are investigated. Accordingly, these models were used in this work and will be described below.

As previously explained, the erosion rate and the penetration ratio are defined, respectively, as:

$$E_f = \frac{1}{A_f} \sum_{\pi(f)} \dot{m}_\pi \, e_r \tag{4.39}$$

$$\text{Penetration Ratio} = \frac{E_f}{\dot{m}_p \, \rho} \tag{4.40}$$

The predictive equation for erosion damage proposed by Oka, Okamura e Yoshida (2005b) can be expressed as:

$$E(\alpha) = g(\alpha) \, E_{90} \tag{4.41}$$

$E(\alpha)$ and E_{90} denote a unit of eroded material per mass of particles ($\text{mm}^3\text{kg}^{-1}$). $g(\alpha)$ is the impact angle dependence expressed by two trigonometric functions and by the initial eroded material Vickers hardness number (Hv) in unit of GPa, as in Eq. (4.42):

$$g(\alpha) = (\sin \alpha)^{n_1} (1 + \text{Hv} \, (1 - \sin \alpha))^{n_2} \tag{4.42}$$

n_1 and n_2 are exponents determined by the eroded material hardness and other impact conditions such particle properties and shape. These exponents shows the effects of repeated plastic deformation and cutting action, and for particles of SiO_2-1 are expressed by:

$$n_1 = 0.71 \, (\text{Hv})^{0.14} \tag{4.43}$$

$$n_2 = 2.4 \, (\text{Hv})^{-0.94} \tag{4.44}$$

The reference erosion ratio E_{90} (erosion damage at normal impact angle) is related to impact velocity, particle diameter and eroded material hardness, and can be expanded

as follows:

$$E_{90} = K\,(a\,\mathrm{Hv})^{k_1 b}\left(\frac{u_p}{u_{ref}}\right)^{k_2}\left(\frac{D_p}{D_{ref}}\right)^{k_3} \tag{4.45}$$

u and D are the impact velocity ($\mathrm{m\,s^{-1}}$) and particle diameter (μm), respectively, and u_{ref} and D_{ref} are the reference impact velocity and the particle diameter used in the experiments by Oka, Okamura e Yoshida (2005b). k_3 is a exponent which take an arbitrary unit and is determined by the properties of the particle. k_2 exponent can be determined by eroded material Vickers hardness and by particle properties, as shown in Eq. (4.46):

$$k_2 = 2.3\,(\mathrm{Hv})^{0.038} \tag{4.46}$$

According to Oka, Okamura e Yoshida (2005b) the term $K\,(a\,\mathrm{Hv})^{k_1 b}$ is highly dependent on the type of the particle and eroded material Vickers hardness which are not correlated with the impact conditions and other factors. The present work used the experimental data from Oka, Okamura e Yoshida (2005b) to derive a function and obtain the relationship between eroded material Vickers hardness and E_{90} at the reference impact velocity. The function obtained by the curve fitting shown in Fig. 2 of Oka, Okamura e Yoshida (2005b) for the pair SiO2-aluminum is provided below::

$$K\,(a\,\mathrm{Hv})^{k_1 b} \approx 81.714\,(\mathrm{Hv})^{-0.79} \tag{4.47}$$

Is important to emphasize that this function is for the pair sand-aluminum and may change for other materials. As a result, E_{90} can be expressed as follows:

$$E_{90} = 81.714\,(\mathrm{Hv})^{-0.79}\left(\frac{u_p}{u_{ref}}\right)^{k_2}\left(\frac{D_p}{D_{ref}}\right)^{k_3} \tag{4.48}$$

The purported strength of the Oka model is that the coefficients for a particular combination of eroded and erodent materials can be derived from more fundamental coefficients. Hence, the fundamental coefficients for sand can serve as a basis for both sand-steel erosion and sand-aluminum erosion, for instance. Table 1 summarizes all the erosion ratio model constants used in the present work.

Grant e Tabakoff (1975) proposed the restitution model after treating the post collisional particle movement dynamics in a statistical approach. Based on experimental data on aluminum and sand, they proposed equations (4.49) and (4.50) for the coefficients:

$$e = 0.993 - 1.76\,\alpha + 1.56\,\alpha^2 - 0.49\,\alpha^3 \tag{4.49}$$

$$e_{par} = 0.998 - 1.55\,\alpha + 2.11\,\alpha^2 - 0.67\,\alpha^3 \tag{4.50}$$

Friction is another important effect to be accounted for in particle-wall interactions. Depending on the static and dynamic coefficients, particles can lose energy and velocity, directly affecting the erosion. In UNSCYFL3D, the standard coefficient was used ($\mu = 0.25$).

Table 1 – Constants used for the erosion ratio correlation.

Eroded material type	Aluminum (6061-T6)
Eroded material Vickers hardness (H_v)	1.049 Gpa
Particle type	Angular SiO_2-1
Reference impact velocity (u_{ref})	104 m/s
Reference particle diameter (D_{ref})	326 μm
k_2	2.3042
k_3	0.19
n_1	0.7148
n_2	2.2945

5 Finite volume discretization

For the current research the UNSCYFL3D code is employed. UNSCYFL3D, amongst many other CFD packages, uses a Finite Volume Method (FVM) in order to resolve a flow field depending on its geometrical boundaries and their respective boundary conditions. For this approach the equations presented in the previous chapter have to be discretized in space. Since the problems is treated in a steady-state form, the discretization in time will not be described in this work.

This chapter presents a brief overview of the discretization methods employed for the current research. It is largely based on the information in the Fluent Guide (2005), supplemented with the work of Ferziger e Peric (2002) and Mathur e Murthy (1997). The methods outlined below may not be optimal, but they have proven to deliver sufficiently accurate results within a reasonable amount of time for the problem at hand.

Section 5.1 introduces the FVM. Then Sections 5.2 present the spatial discretization. The pressure-velocity coupling is presented in Section 5.3 and the solution procedure is elaborated in Section 5.4.

5.1 Finite Volume Method

The Finite Volume Method (FVM) is a method for representing and evaluating partial differential equations in the form of algebraic equations (LEVEQUE, 2002; TORO, 2009). Similar to the finite difference method or finite element method, values are calculated at discrete places on a meshed geometry. In the finite volume method, volume integrals in a partial differential equation that contain a divergence term are converted to surface integrals, using the divergence theorem. These terms are then evaluated as fluxes at the surfaces of each finite volume. Because the flux entering a given volume is identical to that leaving the adjacent volume, these methods are conservative. Another advantage of the finite volume method is that it is easily formulated to allow for unstructured meshes (VERSTEEG; MALALASEKERA, 2007).

5.2 Spatial discretization

The conservation equations for the continuity, velocity components and for the turbulence variables in steady state can be written generically as:

$$\frac{\partial}{\partial x_j}(\rho u_j \phi) = \frac{\partial}{\partial x_j}\left(\Gamma \frac{\partial \phi}{\partial x_j}\right) + S_\phi \tag{5.1}$$

By integrating the general conservation Eq. 5.1 over the control volume V, we obtain:

$$\oint_A \rho\phi\vec{V} \cdot d\vec{A} = \oint_A \Gamma \text{grad}\phi \cdot d\vec{A} + \oint_V S_\phi dV \tag{5.2}$$

Note that, for the terms involving surface integrals in Eq. 5.2, the Gauss Divergence Theorem was applied to convert the volume integrals into surface integrals (FERZIGER; PERIC, 2002):

$$\int_V \frac{\partial \phi}{\partial x_i} dV = \oint_A \phi \vec{l_i} \cdot d\vec{A} \tag{5.3}$$

For the element L shown in Fig. 8, and located at the LHS of face f, the discretization of Eq. 5.3 yields:

$$\sum_f J_f \phi_f = \sum_f D_f + (S_\phi \, \Delta V)_L \tag{5.4}$$

in which J_f is the mass flow rate, $(\rho_f \vec{V_f} \cdot \vec{A_f})$, across face f, Γ_f the diffusion coefficient at the that face and $D_f = \Gamma_f (\text{grad}\phi)_f \cdot \vec{A_f}$ is the diffusive flux across face f. The summations above apply to all the faces of element L. $\vec{A_f}$ is the normal area vector of face f, which is directed from the element L to the element R. Next, the discretization of each term of Eq. 5.4 is detailed.

The advection term

Regarding the advective term in Eq. 5.4, when the first-order upwind scheme is employed, ϕ_f is assigned the value of the element center at element L if J_f is positive. Otherwise, the value of element R is set to the face. Because first-order schemes are usually very diffusive for many applications of interest, a second-order upwind scheme was used in this work:

$$\phi_f = \phi_L + (\text{grad}\phi)_{rL} \cdot \vec{dr}_L \tag{5.5}$$

if $J_f > 0$. If $J_f < 0$ applies Eq. 5.5 considering the element to the right of the face f, R. In the above equation, the value of the variable in the face is obtained by extrapolation of the second order from the value in the *upwind*. The vector $\vec{dr}_L$ is directed from the geometric center of element L to the face f center. $(\text{grad}\phi)_{rL}$ is the reconstructed gradient at element L, which is again computed by means of the Gauss Divergence Theorem:

$$(\text{grad}\phi)_r = \frac{1}{\Delta V} \sum_f (\bar{\phi}_f \vec{A_f}) \tag{5.6}$$

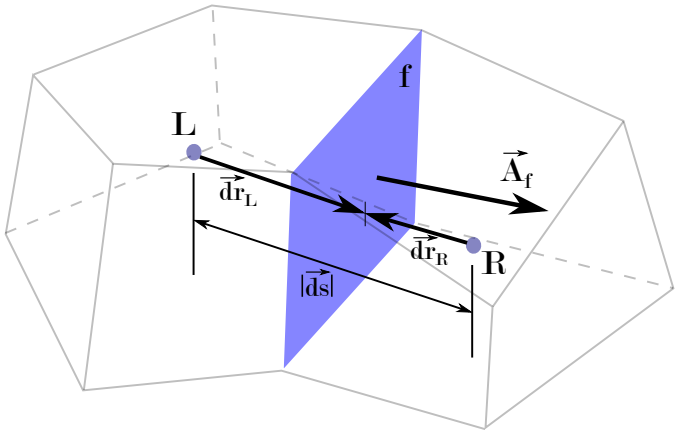

Figure 8 – Control volume for a finite volume discretization.

where $\bar{\phi}_f$ is the average of ϕ the element centers sharing face f.

The first term on the right side of Eq. 5.6 is always implicitly treated, whereas the second term is treated as source term and therefore calculated explicitly.

The diffusion term

It can be proven that the diffusive flux for face f is given by (MATHUR; MURTHY, 1997):

$$D_f = \Gamma_f \frac{(\phi_R - \phi_L)}{|\vec{ds}|} \frac{\vec{A}_f \cdot \vec{A}_f}{\vec{A}_f \cdot \vec{e}_s} + \Gamma_f \left[\overline{\text{grad}\phi} \cdot \vec{A}_f - \overline{\text{grad}\phi} \cdot \vec{e}_s \frac{\vec{A}_f \cdot \vec{A}_f}{\vec{A}_f \cdot \vec{e}_s} \right] \tag{5.7}$$

In Eq. 5.7, $\vec{e}_s$ is the unit vector connecting the centers of elements R e L, $\vec{e}_s = \frac{\vec{ds}}{|\vec{dr}|}$. The first term at the RHS of Eq. 5.7 is treated implicitly, whereas the remaining terms, which represent the secondary diffusion, are calculated explicitly and therefore incorporated into the source-term S in Eq. 5.4. The secondary diffusion is null for hexahedra for instance, because vectors $\vec{A}_f$ and $\vec{e}_s$ are collinear. The gradient at face f, $\overline{\text{grad}\phi}$, is calculated as the average of the gradients at the adjacent elements. The treatment above is equivalent to the application of the second-order, centered differencing scheme in structured meshes and is advantageous in the sense that it does not depend on the element shape.

5.3 Pressure-velocity coupling

So far, it was proved that the momentum equations can be discretized via finite volume in unstructured meshes. Note that the set of Eqs. 4.1 and 4.2 forms a system of four equations (continuity, momentum for u, v and w) and four unknowns (u, v, w and

p), thereby forming a given system. The velocity components must be determined by the respective conservation equations, but restricted with the imposed continuity. There is no explicit equation for the pressure, which requires the deduction of an equation for this variable so a segregated method of solution can be employed. The UNSCYFL3D uses the SIMPLE method (Semi-Implicit Pressure-Linked Equations, (FERZIGER; PERIC, 2002)) to generate this equation and ensure that the continuity equation is also satisfied.

In the SIMPLE method, the procedure solution of the equations for u, v, w and p is said segregated, which means that a system of linear equations for each of these variables are resolved independently by linear system solution methods, and sequentially. The process is repeated until all the standard equations residues is reduced until the specified tolerance. Several global iterations, with the solution of linear systems for u, v, w and p, may be necessary due to the nonlinear nature of the Navier-Stokes equations and the coupling between the variables. Since the variables converge at different speeds, it is necessary under-relaxed the system solutions. For the case of transient problems, global iterations should be performed at each time step, and the process is repeated at each time step.

A more detailed discussion on pressure-velocity coupling can be found in (FERZIGER; PERIC, 2002).

5.4 Solution procedure

For the current study, only steady simulations are performed. For steady simulations the SIMPLE algorithm by Patankar (1980) is employed and briefly discussed below.

The SIMPLE algorithm can be summarized as follows:

1. Start-up the values of the velocities components and pressure in the elements and the mass flow rates across the faces of the calculation area, including the boundaries. These fields do not necessarily satisfy the conservation equations;

2. solves the linear system of equations for each component of the velocity vector, this corresponds to the predictor step. UNSCYFL3D uses biconjugated gradient method;

3. with the predicted velocity field, the mass flow rates is calculated on the faces of all the elements. It is then solved the linear system for the pressure correction. Normally, it is necessary to use an efficient solver based on multigrid methods, for example;

4. by knowing the pressure correction, the mass flow rates are corrected on the faces, the pressure in each element, and the velocity components in each element;

5. evaluate the residues and the momentum equations after the corrector step and if they are satisfied according to the tolerance specified by the user, declares the

convergence of the set of equations. Due to the couplings between the variables, a global iteration of SIMPLE is usually not sufficient to ensure that all equations are satisfied simultaneously. In this case, the solver returns to the step 2 and the process continues until the convergence of all the equations.

It is important to remember that for transient problems, the above procedure is performed for each time step. The flowchart solution of SIMPLE method is shown in Fig. 9:

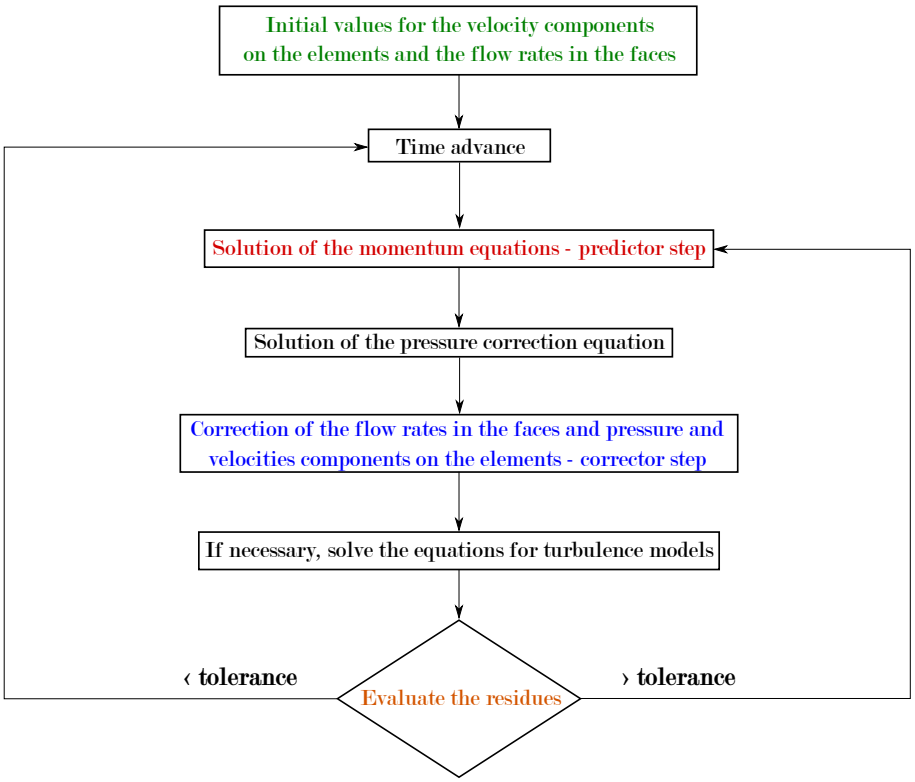

Figure 9 – Flowchart solution of SIMPLE method implemented in UNSCYFL3D.

5.5 Solver UNSCYFL3D

The UNSCYFL3D is an ”in-house” code developed in the Laboratory of Fluid Mechanics (MFlab) from the Federal University of Uberlândia in partnership with PETROBRAS. The code is capable of simulating laminar and turbulent flows with particles. In UNSCYFL3D, the Navier-Stokes equations in the incompressible formulation are solved numerically using the finite volume method of Ferziger e Peric (2002) in unstructured meshes, which can be composed of hexahedra, tetrahedra, prisms, pyramids and wedges. For the disperse phase modeling, a Lagrangian formulation is employed, where the particles are individually tracked in the flow. For the pressure-velocity coupling, the SIMPLE algorithm is used. Flow in both permanent and transient regimes can be simulated, and

6 boundary conditions can be prescribed: imposed velocity, symmetry, outflow, non-slip, imposed pressure and frequency.

The diffusive terms are discretized by 2^{nd} order centered differences, for the advective terms, the *upwind* scheme and the 1^{st} order centered scheme or *upwind* scheme 2^{nd} order can be combined. The large scale turbulence models are: Smagorinsky, dynamic and Yakhot. The SST and DES-SST models are also available. For the integration of the motion equations of the particles, it uses the analytical model previous described in Section 4.2. Particles can be injected into faces in which the boundary condition of imposed velocity is applied. The following boundary conditions for the particles are possible: reflection, escape and frequency.

For the erosion-related problems the correlations from: Ahlert (1994), Neilson e Gilchrist (1968), Zhang et al. (2007) and Oka, Okamura e Yoshida (2005b) can be employed. The coefficients of restitution can be selected from: Forder, Thew e Harrison (1998), Sommerfeld e Huber (1999) and Grant e Tabakoff (1975) models.

For time advance of the flow equations, the implicit Euler scheme 1^{st} and three levels in time 2^{nd} can be used. The mesh converter was developed in C language, and the solver in FORTRAN 90 language. Both flow and particles can be post processed using Paraview and VisIt tools.

6 Particle phase algorithm

According to Elghobashi (1993), when starting a single-phase flow into a flow with a high particle loading, four different regimes will be achieved, and these arrangements relate to the manner in which the flow "feels" the presence of the dispersed phase (type of coupling) and the manner in which the dispersed phase interferes with the turbulence of the continuous phase (attenuating or increasing the turbulence levels).

For both Lagrangian and Eulerian approaches, it should be noted that the two-way coupling requires the description of the coupling between the phases and the particle. This interaction occurs through the tension between the phases at the particle surface. In particular, the coupling strength between the phases is the force acting on a single particle due to pressure and viscous tension caused by the disturbed fluid around. This force is equal in magnitude and opposite in direction to hydrodynamic force of the particle acting on the continuous phase. The coupling strength between the phases is the hydrodynamic forces on the surface less the contributions of the tensions of the undisturbed fluid (*e.g.*, less forces due to the pressure gradients which occur regardless of the presence of the particle).

The next section will briefly explain the coupling procedure used in UNSCYFL3D.

6.1 Coupling procedure

The coupled solution of the continuous and particle phases is summarized as follows (LAíN; SOMMERFELD, 2012): first the steady-state solution for the fluid phase without particles is computed. Subsequently, particles are injected and tracked throughout the domain. For each control volume, the average and RMS linear and angular velocities, the particle concentration and the source-terms for the fluid momentum equation are stored.

After all the particles have left the domain, the fluid flow is solved again, now considering the source-terms sampled during the previous particle calculation. This process is repeated, taking the particle-to-particle collision into account, until a converged solution for both phases is reached. It is important to bear in mind that the particle statistics must be corrected during each particle calculation. Another important detail is that the particle source term must be under-relaxed, for achieving convergence. The present work used 0.1 as under-relaxation factor for all the cases, and the quality of convergence was measured based on the standard deviation of average velocities, which should be close to 0.001. Normally, 100 coupling iterations are sufficient for convergence of both phases. A detailed information about this method is given by (LAíN; SOMMERFELD, 2013).

The scheme of this procedure is presented in Fig. 10.

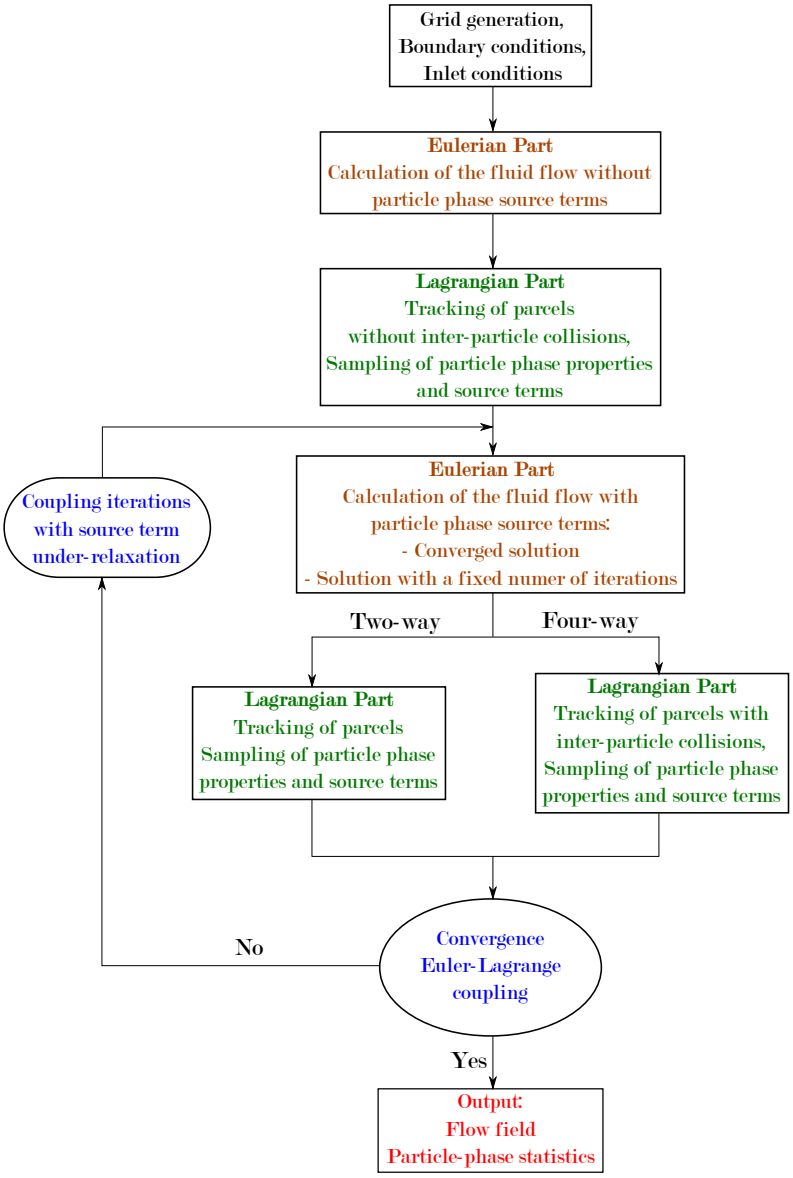

Figure 10 – Flow chart of fully coupled Euler-Lagrange calculations (LAíN; SOMMERFELD, 2013).

To solve the differential equations, it is important to know the location of each particle within the Eulerian mesh. This occurs because to calculate the variation of velocity and position of the particles is necessary to interpolate the fluid properties to the position of its center of mass. Usually, the computational determination of the cell in which a particle is can be done quickly and efficiently by using a particle locator and a mesh mapping in cartesian uniform meshes. However, this approach can not be directly used in unstructured grids (PENG et al., 2009), making the particle tracking problem an important element. Next section is dedicated to briefly explain the particle-location algorithm used in the present report.

6.2 Particle-tracking algorithm

The UNSCYFL3D code uses the algorithm proposed by Haselbacher, Najjar e Ferry (2007). This choice was due to some specific features of this algorithm:

- this algorithm is robust enough to allow a particle to crosses more than one computational cell in a single step and time, in other words, the algorithm enables the particle to go through long distances, which is a limiting factor for a number of algorithms;
- the algorithm is based on distances intersection rather than time intersection, which is much more natural, once the particle tracking problem should be primarily a spatial problem, not temporal;
- the algorithm can be applied to Eulerian meshes consisting of polyhedral elements;
- according to the author, this algorithm is faster and more efficient than other published algorithms.

The complete procedure of particle-location as well as the algorithms used are not presented here because it differ completely from the main theme of the dissertation. A detailed information about the algorithm and its implementation can be found in the publication of Haselbacher, Najjar e Ferry (2007).

All the information presented until now allow the reader to familiarize themselves with the problem analyzed and the procedure used for its solution. With this in mind, will be presented in the following chapters the numerical setup and procedure (Chap. 7) and the results (Chap. 8) obtained, respectively.

7 Numerical setup and procedure

According to the experiment configuration described by Mazumder, Shirazi e McLaury (2008), which aluminum elbow specimens were used, sand particles were injected in the horizontal line at about 1.22 meters below the test piece. The test piece was a 90° elbow with a diameter of 0.0254 meters (D) and a curvature radius of 0.0381 meters. The erosion profile were measured along the outer bend surface as shown in Fig. 11. Hence a comparison of the calculations with the measurements is also made for this location. In order to represent more realistic behavior at the specimen location, wthe hole domain was included on the calculation, attempting to better reproduce the experimental conditions.

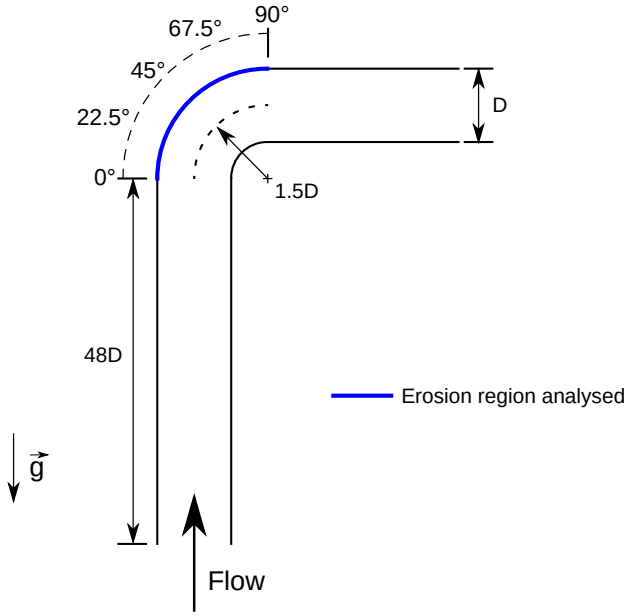

Figure 11 – Schematics of the elbow investigated.

At the inlet of the pipe, the fluid is injected with a mean conveying velocity of 34.1 m/s and a turbulence intensity of 5%. At the pipe walls a no-slip condition is applied whilst at the pipe exit an outlet condition is adopted. Table 2 summarize all the properties of the fluid, particle and pipe used in all computations. These conditions yield a pipe Reynolds number of 5.93×10^4 and a particle Stokes number based on the averaged diameter of 3.66.

Regarding the two-phase flow simulations, the mass loading ratio considered in the experimental measurements was $\phi = 0.013$. After the validation for the experimental mass loading, higher mass loadings computations were carried out in order to quantify its effect in the flow and in the penetration ratio. For all cases studied, the mean particle diameter was 182 μm and the pipe material was Aluminum (6061-T6). The pipe wall

Table 2 – Simulation conditions for erosion prediction.

Fluid	Air
Fluid density	$1.225\,\mathrm{kg/m^3}$
Fluid viscosity	$1.79 \times 10^{-5}\,\mathrm{Pa.s}$
Fluid velocity	$34.1\,\mathrm{m/s}$
Material of specimen	Aluminum (6061-T6)
Material density	$2,700\,\mathrm{kg/m^3}$
Pipe diameter (D)	$0.0254\,\mathrm{m}$
Elbow curvature ($1.5D$)	$0.0381\,\mathrm{m}$
Particle type	Angular SiO_2-1
Particle density	$2,600\,\mathrm{kg/m^3}$
Average particle size	$182\,\mu\mathrm{m}$
Mass loading	$0.013, 0.25, 0.5, 1.0, 1.5\,\mathrm{kg}_p/\mathrm{kg}_g$

roughness angle distribution has been chosen to be $\Delta\gamma = 0°$ (perfectly smooth). For the particle phase simulation, $250,000$ computational particles were tracked through the flow field during the coupling iterations. At the final step, about twelve million computational particles were simulated in order to obtain a statistically converged field. It is important to bear in mind that each computational particle represents a number of real particles with same properties (*e.g.*, velocity and size) becoming different when the mass loading is changed.

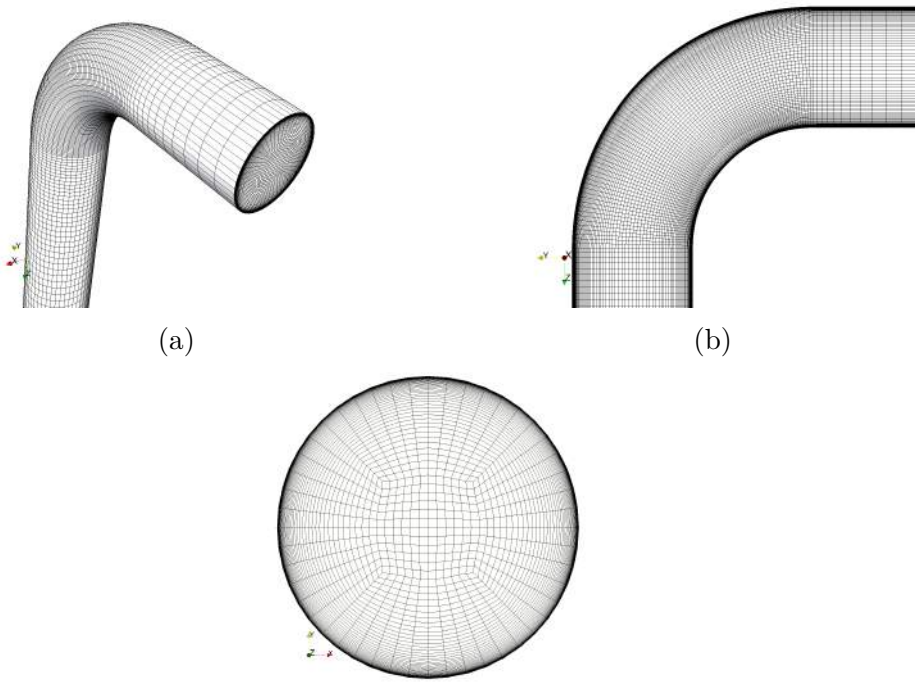

(a) (b)

(c)

Figure 12 – Standard Elbow domain.

The grid refinement was performed using only hexahedral elements, which implies in more stability and generates less numerical diffusion in the simulations. This type elements offers the possibility of gradual refinement near the walls Fig. 12c, where great velocity gradients and boundary layer do exist. As a consequence, this sort of element generates higher quality meshes, with fewer distorted elements than one would obtain with tetrahedral, for example. The mesh resolution used in all standard elbow simulations is approximately 500,000 elements, which was found to produce grid-independent results Figs. 12a and 12b.

After simulate all the cases under the above-mentioned circumstances, a vortex chamber was added to the standard geometry. The main geometric characteristics (i.e pipe diameter, curvature radius, domain size) and simulation conditions were maintained, the major modification was the creation of a semi sphere at the opposite side of the inlet domain. In order to keep the geometric fidelity, the diameter of this semi sphere need to be lightly larger than the pipe diameter, this provides the structural form responsible to force the fluid flow to rotate inside the chamber. As a result, it was used a semi sphere with a diameter of 0.036 meters which can be seen in Fig. 13. Moreover, to quantitatively compare the vortex-chamber elbow penetration ratio with the standard elbow results, a penetration ratio profile was extracted from a middle plane in the longitudinal direction of the vortex chamber. Since the vortex chamber represents the most susceptible region for particle-wall collisions, it is reasonable to compare this eroded region with the one mentioned above for the standard elbow.

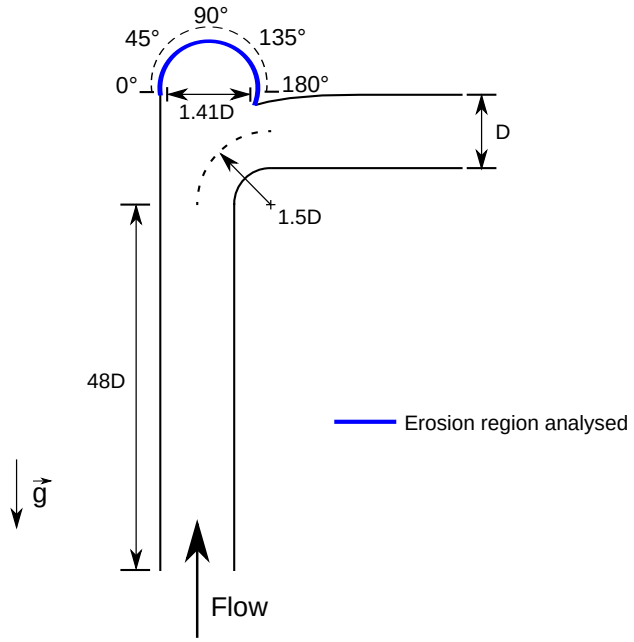

Figure 13 – Schematics of the vortex-chamber elbow investigated.

The grid generation of the vortex-chamber elbow follow the same steps of the

standard elbow. The grid refinement near the walls was preserved Fig. 14c, as well as the less distorted elements inside the vortex chamber Fig. 14b. To easily generate the vortex chamber mesh, an multi-block structured grid with an O-type structure composed of 5 blocks was used resulting in a total of 670,000 hexahedral control volumes.

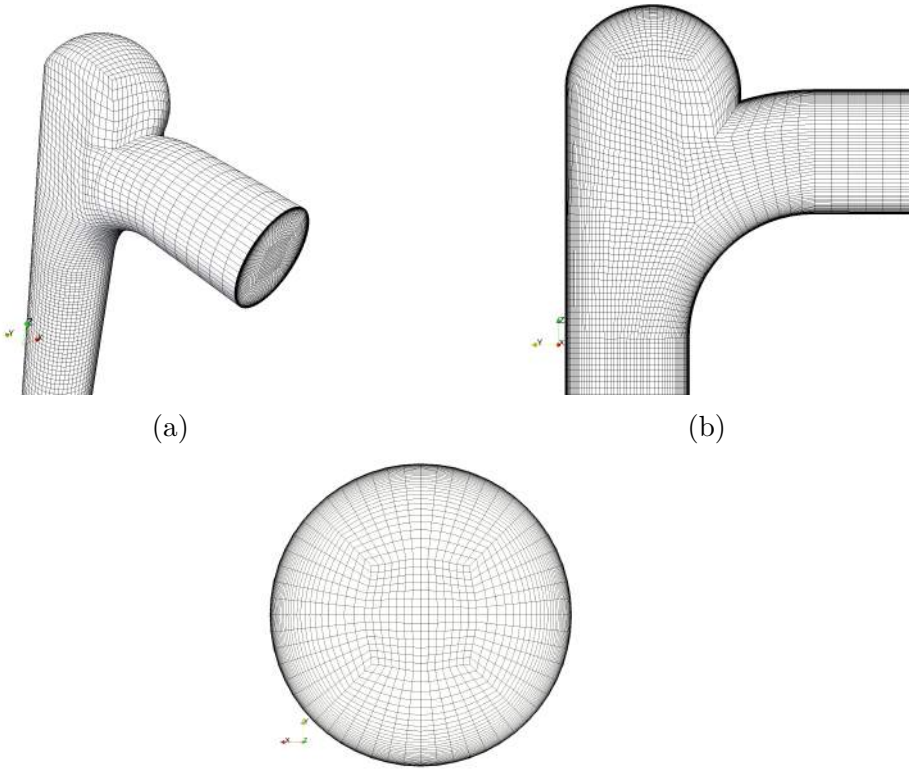

(a) (b)

(c)

Figure 14 – Vortex-Chamber Elbow domain.

8 Results

The results section is divided in two main sections. Section 8.1 show the results for the standard elbow case. This section provides a detailed information about the effects that changes the erosion profile due to the increase of the mass loading which is the key to understand the mechanisms of erosion reduction. Section 8.2 is dedicated to explain the flow dynamics and the particle interactions responsible to reduce the erosion in vortex-chamber elbows. Finally, a comparison between both elbows erosion is made and remarkable results are presented.

8.1 Standard elbow results

Figure 15 shows the streamlines of the velocity field inside the standard elbow. This figure illustrate the fluid behavior inside the bend and give an initial idea about the studied problem.

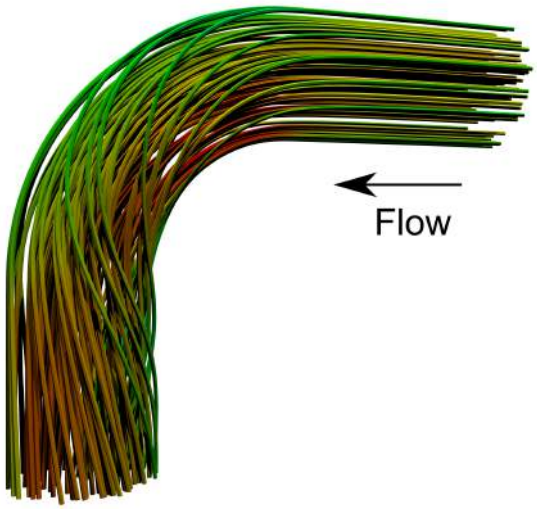

Figure 15 – Streamlines of the velocity field inside the standard elbow.

8.1.1 Validation at low concentration - One, two and four-way couplings

First, to provide an overview of the effects of mass loading on the penetration ratio, two cases were analyzed. As mentioned in Section 4.3 the friction coefficient was set as 0.25 and the restitution model of Grant e Tabakoff (1975) was chosen. Because this restitution model was originally obtained from experiments with sand particles hitting against an aluminum surface, it is the most appropriate correlation for the current investigations.

The first test conducted in this work aims at validating the numerical results using the experiments carried out by Mazumder, Shirazi e McLaury (2008). The original experiment was performed at low mass loading ($\phi = 0.013$), and the contours of the penetration ratio for one, two and four-way couplings, seen from the opposite side of the inlet domain, are shown in Fig 16. It can be seen that, irrespective of the interaction regime, the contours of erosion are very similar, as well as the magnitude of the penetration ratio, quantitatively speaking. This general behavior was expected, since the mass loading is low enough not to cause significant coupling between the two phases.

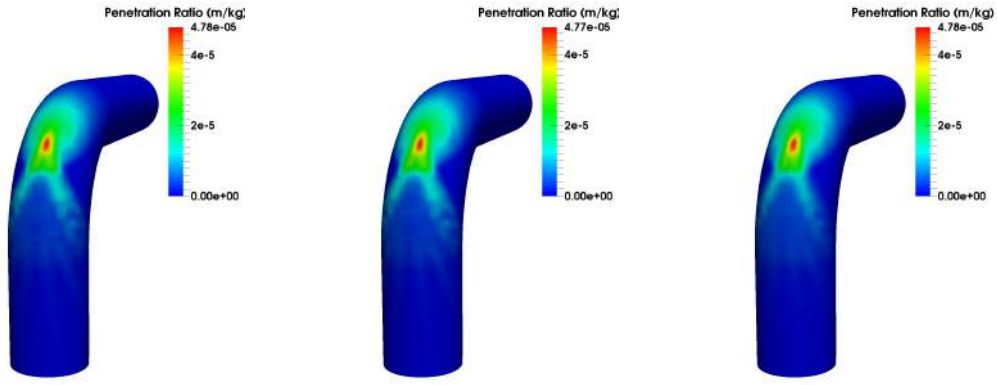

(a) (b) (c)

Figure 16 – Erosion contours of mass loading $\phi = 0.013$ with different levels of interaction: (a) One-way coupling; (b) Two-way coupling; (c) Four-way coupling.

Based on the experimental data, it was also possible to quantitatively compare the erosion profile in the outer wall of the elbow as a function of the curvature angle. The origin (0°) is set at the elbow inlet, and 90° corresponds to the elbow flow outlet (Fig. 11). Figure 17 shows the penetration ratio profile for one, two and four-way couplings, as well as the experimental data by Mazumder, Shirazi e McLaury (2008) which also display the range of variation for each experimental point (each point was measured three times).

An analysis of Fig. 17 reveals that, independently of the interactions considered in the simulation, for the mass loading of $\phi = 0.013$, the model produces accurate results when compared to the experiment. Up to this point, one-way coupling model would have been sufficient to reproduce the experiment and to yield good results. Obviously, one-way coupling implies in much lower computational cost and a considerable reduction in simulation time. However, as will be demonstrated further, caution is necessary about the choice of the coupling model. As the mass loading increases, neglecting interaction with the fluid and inter-particle collisions may generate inaccurate results.

With the purpose of observing the effect of the coupling models in both phases, a second test was conducted. The problem setup is identical to the previous one, but with the mass loading set to $\phi = 0.25$. Figure 18 illustrates the contours of penetration ratio

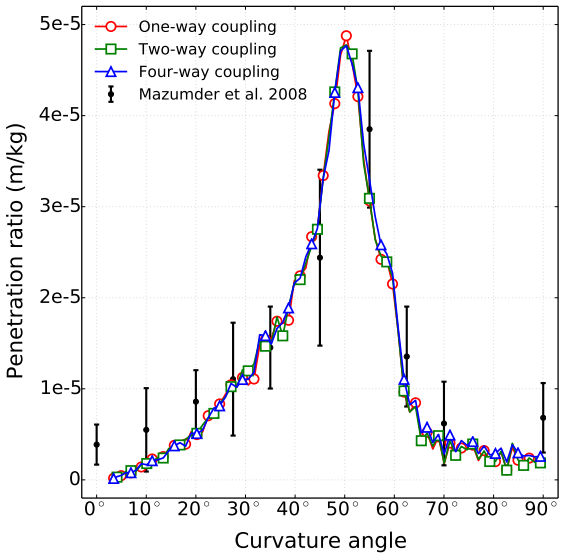

Figure 17 – Numerical and experimental penetration ratios versus bend curvature angle for one, two and four-way couplings. Mass loading $\phi = 0.013$.

for the second test. Despite the relatively low mass loading ($\phi < 1$), the penetration ratio contours for the four-way calculation (Fig. 18c) is observed to be significantly different from those obtained assuming only one-way (Fig. 18a), and two-way (Fig. 18b) couplings. The four-way coupling results show an extended region of maximum penetration and a gradual softening around that location, whereas for one and two-way couplings, the shape of the penetration ratio remains similar.

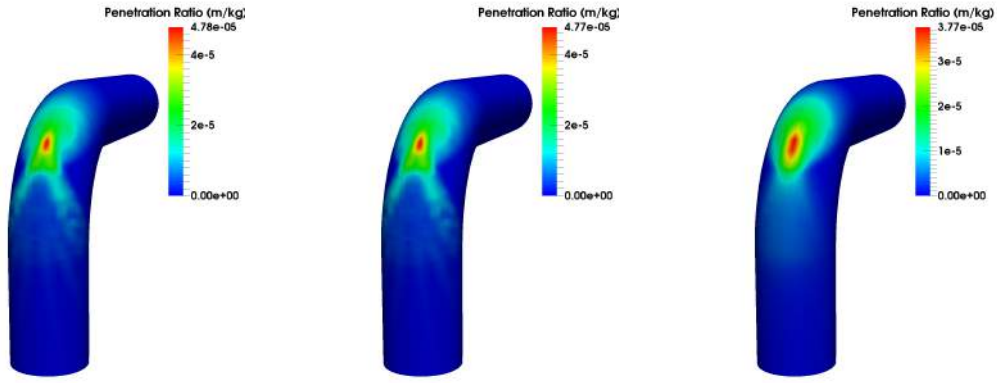

(a) (b) (c)

Figure 18 – Erosion contours of mass loading $\phi = 0.25$ with different phase interaction regimes: (a) One-way coupling; (b) Two-way coupling; (c) Four-way coupling.

In this case, it is evident that the inter-particle collisions can directly influence the erosion profile and cannot be ignored. This behavior can be seen in Fig. 19. It can be observed from the erosion profile, that the two-way coupling results remain nearly

identical to the one-way coupling results. This means that the particles do not provide or extract enough momentum to alter the mean gas flow properties or its turbulence structure. Although the mass loading is greater than that of the first test, it is important to have in mind that these particles are rather inertial. Consequently, they not expected to be very sensitive to the continuous phase turbulence. Up to this point, it can be concluded that the collisions between particles are responsible for reducing the maximum penetration ratio magnitude in the elbow.

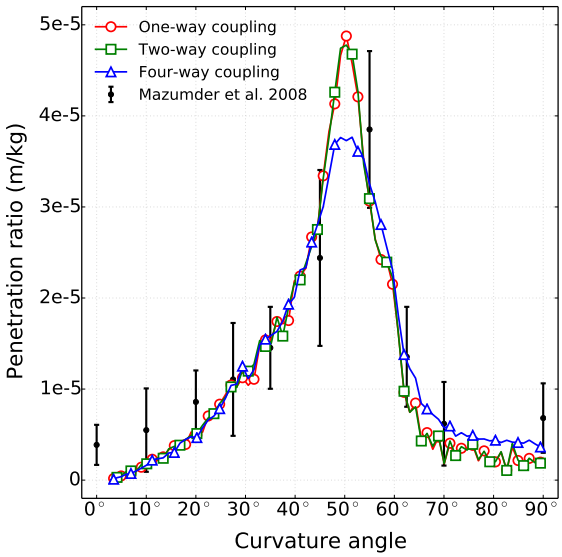

Figure 19 – Numerical and experimental penetration ratio versus bend curvature angle for one, two and four-way coupling and mass loading $\phi = 0.25$.

The four-way calculation indicates how significant the inter-particle collisions can be. The regions between 45° and 55°, display a significant reduction of the penetration ratio peak (approximately 23 %). Another region, between 60° and 90°, on the other hand, show that the penetration ratio is slightly increased.

Essentially, the results suggest that the inter particle collisions actually protect the elbow surface from the direct impact from the incoming particles at the maximum penetration location. Since the penetration ratio is cumulatively calculated, each individual collision contributes to the erosion damage. Apparently, because of the inter-particle collisions, the effective number of particles colliding with the wall in the maximum penetration region is reduced, although an increase is visible downstream of such region. Because of the local high particle concentration, there is an increase of particle-to-particle collision in the maximum impact region, which actually seems to shield the eroded surface. This phenomenon is outlined in Section 8.1.4.

An important conclusion of this first analysis is that the influence of inter-particle collisions is important even at relatively moderate mass loadings, as demonstrated by

Souza, Silva e Utzig (2014) and Laín e Sommerfeld (2013).

In the next sections, the influence of the interaction of the particles with the carrier fluid and among themselves, the effects of the mass loading on the penetration ratio and the mechanisms related to the cushioning effect will be analyzed.

8.1.2 Two-way versus four-way coupling

Before attempting to understand the effects of increasing mass loadings on the erosion, a comparison between results for two (lines with symbols) and four-way (dashed lines) for two different mass loadings is made in Fig. 20.

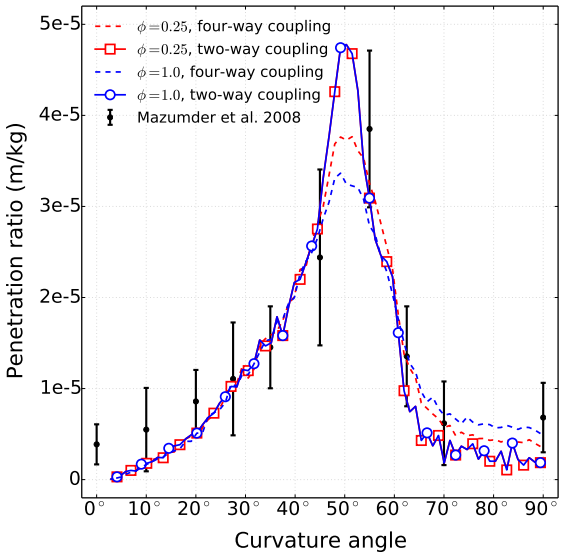

Figure 20 – Influence of two-way (lines with symbols) and four-way (dashed lines) coupling for $\phi = 0.25$ and $\phi = 1.0$.

It can be concluded that in two-way coupling the penetration ratio is exactly the same for the mass loadings of $\phi = 0.25$ and $\phi = 1.0$. This demonstrates that even at higher mass loading, the particles do not significantly affect the gas flow enough to cause changes in the penetration ratio.

However, in the four-way coupling case, a characteristic reduction in penetration ratio is observed when the mass loading is increased. This finding corroborates the conclusions of the previous section: the particle-to-particle collisions play the most important role in attenuating the erosion peaks.

It has been shown in a number of papers (LAíN; SOMMERFELD, 2012) that the inter-particle collisions tend to make both particle and gas flows more homogeneous by flattening the velocity profiles in the pipe cross-section. Since the erosion rate is directly proportional to a power of the impact velocity (*cf.* Eq. 4.48), a reduction in the penetration

might be due to the particle velocity reduction when the inter-particle collisions are taken into account. Nevertheless, Fig. 21 shows that the average particle axial velocities in the two-way (circular symbols) and the four-way couplings (square symbols) in the fully developed pipe region are quite similar. There is a slight reduction in the particle velocity in the center of the pipe, whereas an increase is observed close to the walls when inter-particle collisions are considered. However, as previously shown, the penetration profiles for both cases are nearly the same. Consequently, this profile change per se is not responsible for the reduced penetration peak observed.

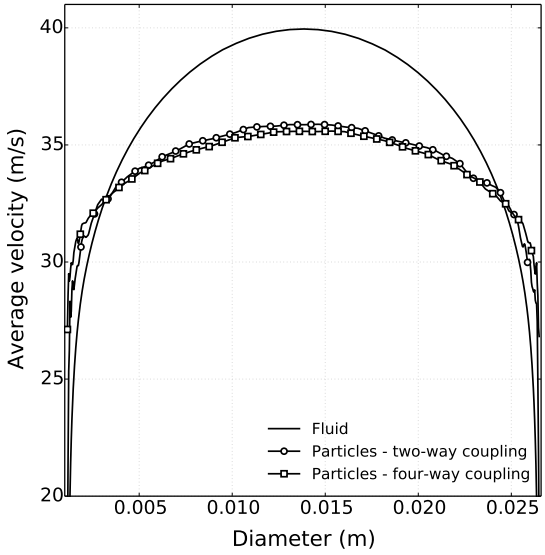

Figure 21 – Average velocity field for the fluid (continuous line), particles in two-way coupling (circles) and particles in four-way coupling (squares). Mass loading is $\phi = 1.0$.

It is important to bear in mind that for pipelines long enough for achieving fully developed flow and at high mass loadings, the reduction of the particle velocity due to collisions can be so significant that renders one and two-way approaches inappropriate. This in turn, directly affects the erosion behavior predicted, especially when collisions between the abrasive particles are the most important mechanisms to explain the phenomenon.

8.1.3 Influence of the mass loading in the penetration ratio

Mass loading is a variable that has been investigated in a few works on erosion. The main advantages to analyze mass loading instead of particle concentration resides in the fact that the former is a dimensionless quantity and its value does not change with the conveying air velocity or pressure, remaining essentially constant along the length of a pipeline.

In order to investigate the influence of the mass loading, five cases with ϕ equal to 0.013, 0.25, 0.5, 1.0 and 1.5 respectively, were then run to assess their effect in the penetration ratio. Naturally, all cases considered particle-to-particle collisions. Figure 22 displays the penetration ratio as a function of the curvature angle for the five cases studied.

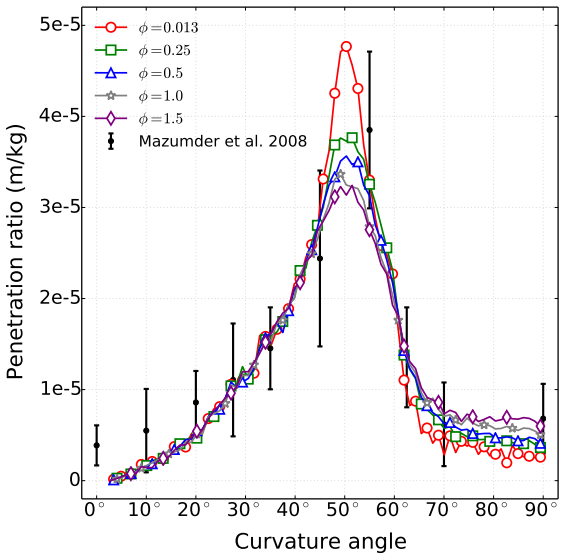

Figure 22 – Influence of the mass loading in the penetration ratio.

The gradual reduction in the peak of the penetration ratio with the mass loading increase, known as cushioning effect, is clearly noticed. Visually speaking, the penetration ratio peak exponentially decays as the mass loading increases, which agrees with the findings of Mills (2004). Somehow, this behavior contradicts the common sense, since it was expected that the injection of a larger amount of erosive particles would result in a higher penetration ratio.

The physical explanation for this reduction is entirely related to the inter-particle collisions, as mentioned in previous sections. As the mass loading increases, more inter-particle collisions occur and less particle-to-wall collisions take place, especially in the peak region of the penetration ratio. The layer of particles immediately adjacent to the wall damps the impact of incoming particles to the elbow surface, reducing the magnitude of the penetration. This has been named "cushioning effect". This effect has been observed experimentally (BIKBAEV et al., 1979), but has not been captured by simulations, to the best of the author knowledge. The region between 0° and 45° of Fig. 22 shows no modification with the increase of the mass loading, which suggests that the particle-to-particle collisions do not significantly affect the particle velocity upstream of the bend.

Figure 23 shows snapshots of a pulse of particles before and during the first collision with the elbow in one (Figs. 23a, 23b, 23c), two (Figs. 23d, 23e, 23f) and four-way (Figs.

23g, 23h, 23i) couplings, for a mass loading of $\phi = 1.0$. Before the first impact, the particles display a characteristic parabolic profile (Figs. 23a, 23d, 23g) and only small differences in these profiles are observed in the four-way coupling case. The inter-particle collisions cause more dispersion in the particle distribution at the main impact region and downstream of it. A distinct change in the particle path is visible during the impact with the wall. Noticeably, the particle-to-particle collisions homogenize the particle distribution upstream and downstream of the main impact region.

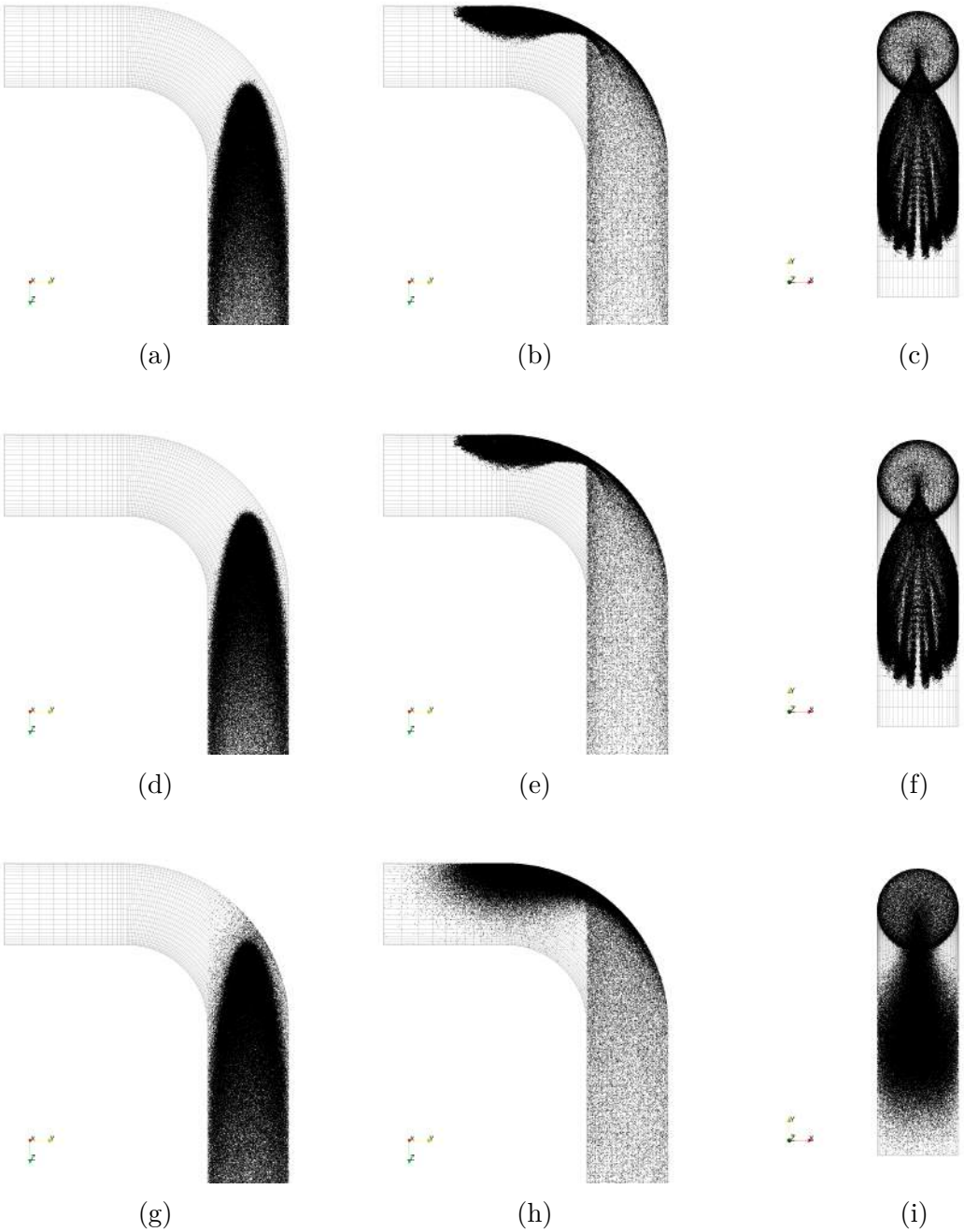

Figure 23 – Snapshot of particle behavior for $\phi = 1.0$. From top to bottom: one-way, two-way and four-way couplings. From left to right: before collision with the bend outer surface, during collision with bend, and during collision with the wall, as seen from the side opposing the inlet domain.

The penetration ratio contours for each mass loading of Fig. 22 are presented in Fig. 24. It can be seen that the extension of maximum penetration is enlarged as the mass loading increases. This a consequence of the more homogeneous particle distribution upstream of the elbow, as shown in Fig. 24.

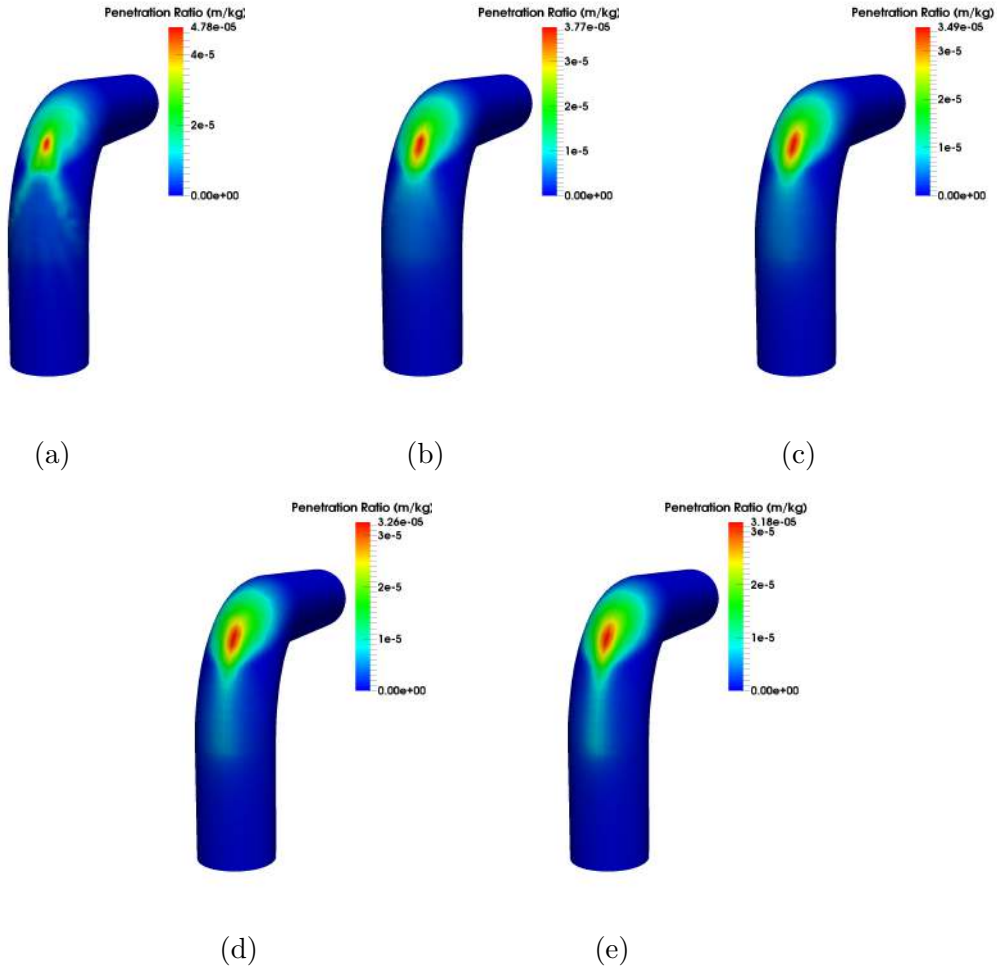

Figure 24 – Erosion contours with four-way coupling approach for the growing mass loadings: (a) $\phi = 0.013$; (b) $\phi = 0.25$; (c) $\phi = 0.5$; (d) $\phi = 1.0$; (e) $\phi = 1.5$.

Another distinctive feature is the modification of the inverted-V shape observed at the lowest concentration. As the particle-to-particle collisions become more relevant, a line with increasing penetration becomes visible downstream of the elbow. A mechanical explanation for such phenomenon can be as complex as that for the rope formation in bends, and results directly from the enhanced inter-particle collisions.

The contours in Fig. 24 suggest that, after the first-colliding particles directly impact the elbow, they are reflected back to the core flow, resulting in particle interactions that prevent some of the incoming particles to reach the maximum erosion region. Instead, these incoming particles are deflect to different locations, especially downstream of the erosion peak. These interactions contribute significantly to change the erosion profile, reducing the maximum penetration ratio, but increasing it at new locations.

It is noteworthy that this study attempts to reproduce an experiment in which the flow is upward. Different erosion patterns may occur depending on the bend orientation, but this is out of the scope of this work and will be investigated in the future.

8.1.4 Mechanisms of particle interactions - Cushioning effect

As mentioned above, the gradual decrease in the penetration ratio related to the increase of the mass loading occurs in a region of the elbow between 45° and 60°. It was also confirmed that this behavior is a consequence of the particle-to-particle collisions. Despite this protecting action, a drawback of the cushioning effect was observed, which is the penetration increase between 60° and 90°. The basic mechanism for the protective effect has already been proposed in Sec. 8.1.3, but the penetration augmentation downstream of the bend is not obvious. It might be speculated that the incoming particles collide with the ones reflected by the particle layer adjacent to the region of maximum erosion, providing them with more momentum. This effect in turn causes more energetic collisions with the region downstream of the elbow, resulting in an erosion increase.

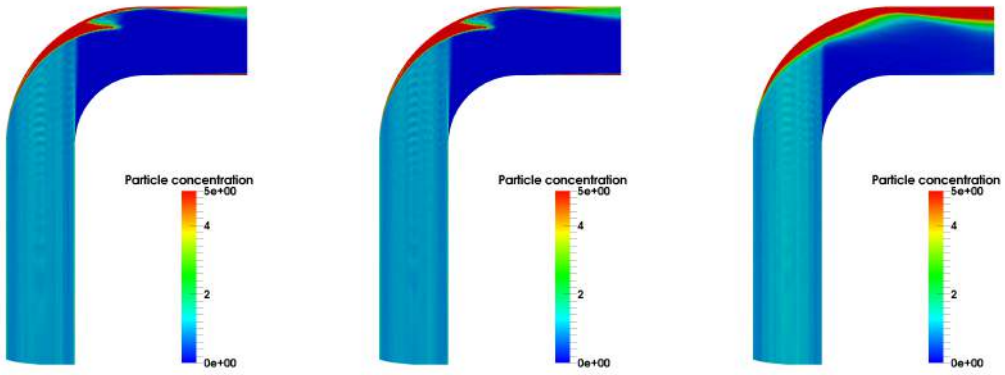

(a) (b) (c)

Figure 25 – Particle concentration field for mass loading $\phi = 1.0$: (a) One-way calculation; (b) Two-way calculation; (c) Four-way calculation.

In Fig. 25 a section in the longitudinal direction of the elbow shows the regions of higher particle concentration for a mass loading of $\phi = 1.0$. It can be seen that, regardless of the coupling model, all concentration contours are virtually the same up to approximately 45°. Downstream of this position, the inter-particle collisions cause the particles to accumulate along the outer bend surface, unlike the particle distribution in one and two-way couplings. In the absence of inter-particle collisions, particles tend to fill up the pipe diameter and move towards the inner part of the bend downstream of the highest penetration region. As a consequence of these sliding collisions at lower velocities, the contours of the penetration ratio as well as the concentration display the inverted-V shape.

In fact, for the one-way (Fig. 25a) and two-way (Fig. 25b) calculations, the concentration profile suffers a sharp discontinuity at a curvature angle close to 60°.

When particle-to-particle collisions are included in the model, the above described particle motion is somehow inhibited. Instead of moving downwards along the pipe walls, the particles rebound from the main impact region actually collide with incoming particles. This effect, in turn, appears to push these particles back to the bend outer wall, which explains the high concentration downstream of the elbow along the pipe upper wall. This is also in accordance with the erosion patterns shown in Fig. 24 for higher mass loadings. Indeed, the particle-to-particle collisions are more elastic than the the particle-to-wall collisions (the coefficient of restitution for the inter-particle collisions is 0.9).

8.2 Vortex-chamber elbow results

8.2.1 Fluid phase simulation

Before discussing about the particulate phase and its effects on erosion profile, the fluid field is presented. Figure 26 shows the streamlines of the velocity field in the region of the vortex chamber. As expected, the flow does not suffer disturbances upstream of the chamber, while it is separated, on the wedge of the vortex chamber, downstream of the elbow. As a consequence, the well defined rotating vortex is generated inside the chamber.

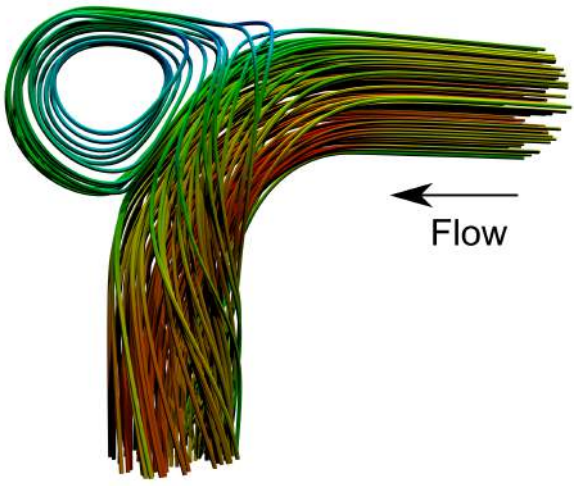

Figure 26 – Streamlines of the velocity field inside the vortex-chamber elbow.

The contours of the velocity magnitude and turbulence kinetic energy are presented in Fig. 27 for the symmetry plane. Within the first 30 degrees past the entrance of the vortex-chamber elbow, the flow adjusts to the transverse pressure gradient imposed by the rotating flow inside the chamber and the location of the maximum velocity is shifted

toward the inner wall. About half-way through the elbow, the velocity contours show a region of high velocity gradients near the inner wall. On the other hand, from the center of the vortex chamber to about a diameter of the elbow entrance, the flow exhibits low velocity gradients. This region is called deflection zone and will be treated in details in section 8.2.2. As the flow exits and continues downstream in the pipe, it is no longer affected by the transverse pressure gradient of the vortex chamber. This results in a shift of the velocity maximum toward the outside wall.

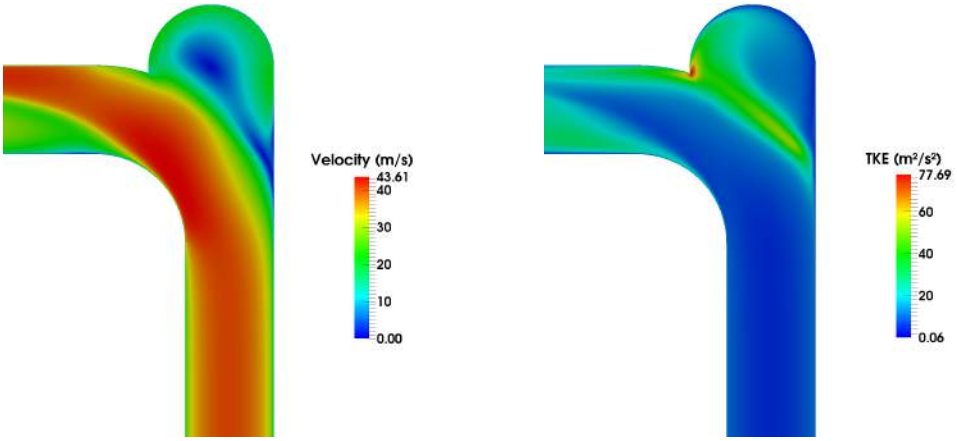

(a) (b)

Figure 27 – Contours of velocity magnitude (a) and turbulence kinetic energy (b) in symmetry plane.

The contours of turbulence kinetic energy (TKE), presented in Fig. 27b, are consistent with those of the velocity magnitude shown in Fig. 27a. As expected, the regions with abrupt velocity gradients are associated with high values of velocity fluctuation thus high values of turbulence kinetic energy.

8.2.2 Effects at low concentration - One, two and four-way coupling

Although there is no experimental data regarding the erosion process in vortex-chamber elbows, the validation for the standard elbow presented in Section 8.1.1 proved to be very accurate and will serve as a reference to predict the erosion effects on the vortex-chamber elbow. With this in mind, all the results discussed below will use the same models of erosion and restitution as well as its coefficients and material constants. Then, a plausible comparison between both elbows can be performed.

The first test conducted aimed to evaluate the effects on the erosion profile for both $\phi = 0.013$ and $\phi = 0.25$ mass loadings. As stated before, $\phi = 0.013$ represents the experimental mass loading of the standard elbow (MAZUMDER; SHIRAZI; MCLAURY, 2008). Figure 28 shows the erosion contours for the mass loading $\phi = 0.013$ with one (Fig. 28a), two (Fig. 28b) four-way (Fig. 28c) coupling. Qualitatively speaking, all coupling

approaches show similar characteristics, but the magnitude of penetration in the four-way coupling is slightly lower than the others.

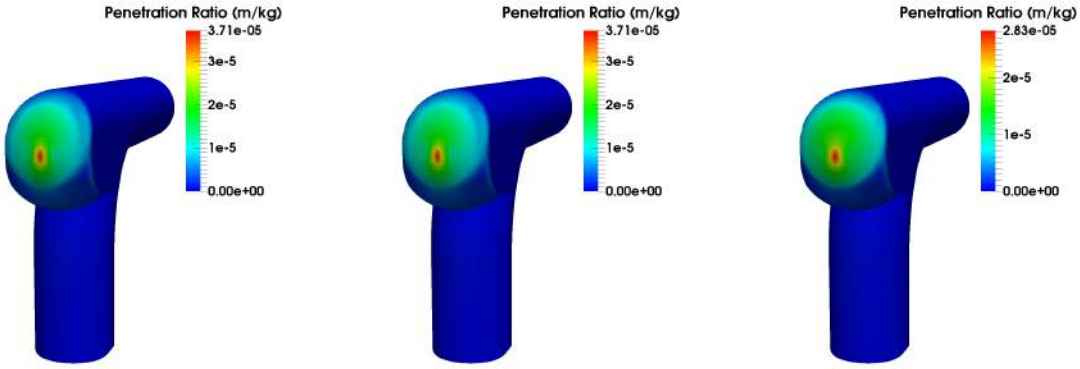

(a) (b) (c)

Figure 28 – Erosion contours of mass loading $\phi = 0.013$ with different phase interaction regimes: (a) One-way coupling; (b) Two-way coupling; (c) Four-way coupling.

This reduction becomes evident when the erosion profile of the outer wall is observed (Fig. 29). For one and two-way coupling there are no significant variations in penetration ratio profile. This reveals that for two-way coupling, the continuous phase is not impacted by the discrete phase, and vice versa. When the collisions between particles are included the profile significantly reduces in all regions of the chamber. The peak of the penetration ratio occurs at 92°.

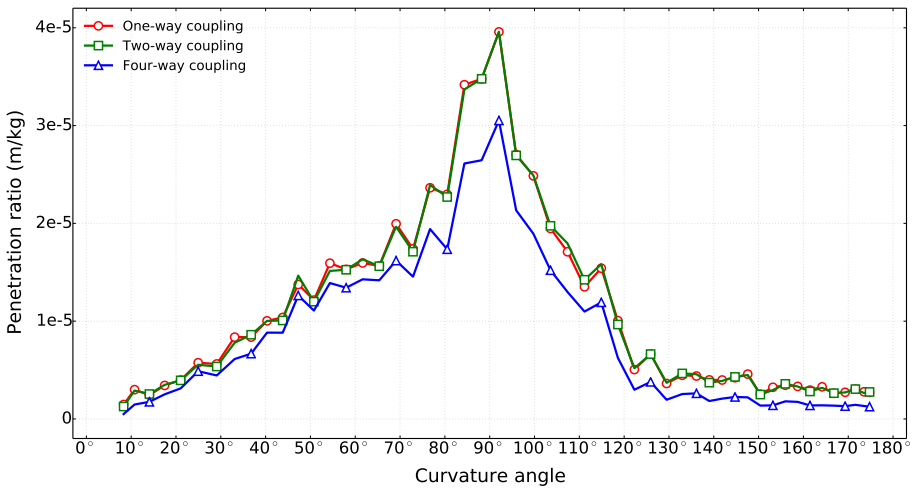

Figure 29 – Numerical penetration ratio versus bend curvature angle for one, two and four-way couplings. Mass loading $\phi = 0.013$.

This preliminary result confirms what was expected, particles are rotating inside the vortex chamber and the collision between them is probably preventing incoming particles to reach and increase the penetration ratio on the chamber wall. Despite the relatively low

mass loading employed, it is notable the importance of using four-way coupling approach for this type of elbow. In this case, collisions between particles plays a decisive role in the erosion reduction. Compared to the same mass loading of the standard elbow (Fig. 17), a penetration peak reduction of 35.9% is observed. In the case of an initial test, the vortex-chamber elbow demonstrated a significant decrease in the penetration ratio and indicates that the results are promising.

In order to quantify the erosion effects due to the increase of the mass loading, a second test with $\phi = 0.25$ was carried out and its contours for each type of coupling approach are shown in Fig. 30.

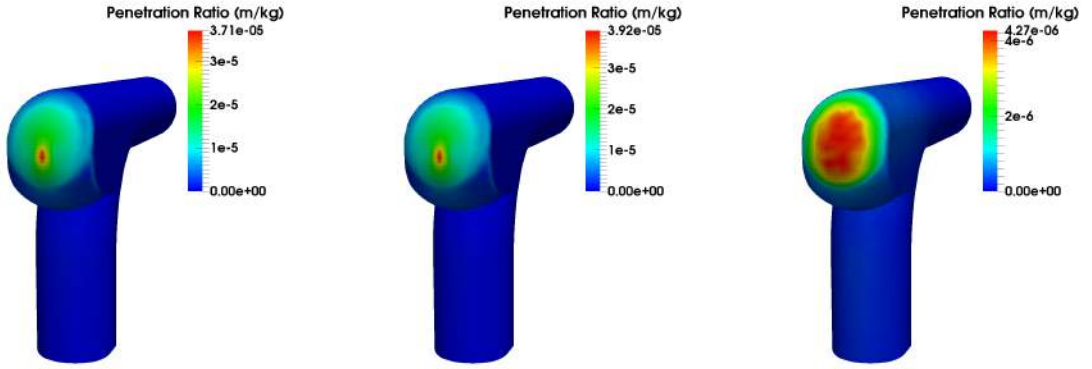

(a) (b) (c)

Figure 30 – Erosion contours of mass loading $\phi = 0.25$ with different phase interaction regimes: (a) One-way coupling; (b) Two-way coupling; (c) Four-way coupling.

For this case, no visible changes are seen in one (Fig. 30a) and two-way (Fig. 30b) coupling approaches, but the penetration ratio magnitude is slightly higher in the last one. Surprisingly, in four-way (Fig. 30c) coupling, the contours change drastically. The region of maximum penetration ratio is notably expanded but its magnitude is greatly reduced. This is the first indication of an effective relation between the increasing of the mass loading and inter-particle collisions in the reduction of the penetration ratio.

To quantify the previous contours reduction, Fig. 31 shows the profiles for each coupling regime. Interestingly, as mentioned above, the peak penetration approach for two-way coupling has a slightly larger peak when compared to one-way. Although the difference is very subtle in the region between 84° and 92°, it can be stated that the fluid is adding momentum in the particles which contributes to increase their velocity and consequently the penetration ratio. Despite being very inertial particles, after suffering the first collision to the chamber, the particles are forced by the prevailing velocity gradients inside the chamber. This directly affects the exchange of momentum between both phases and can not be captured with one-way coupling approach.

However, in the four-way coupling case, an impressive reduction in penetration ratio

is observed. By turning the particles collisions on, the peak reduction was 89.72% compared to two-way coupling calculation. This effect proves that the inter-particle collisions are the most important mechanism in attenuating the penetration ratio in this type of elbow.

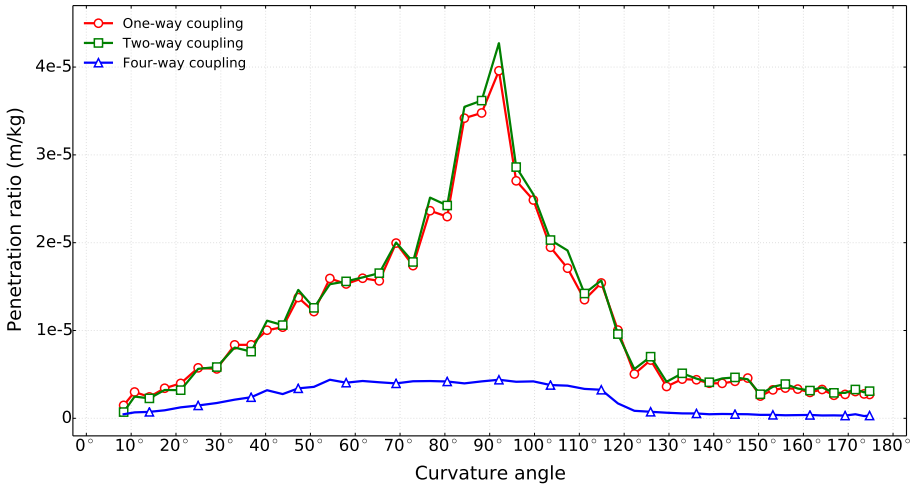

Figure 31 – Numerical penetration ratio versus bend curvature angle for one, two and four-way couplings. Mass loading $\phi = 0.25$.

Before showing the influence of different mass loadings in the penetration ratio, Section 8.2.3 gives an explanation of the effects observed when using only a two-way coupling approach. This analysis provides us with valuable information on how the phases exchange momentum between each other and how this influence the erosion profile.

8.2.3 Two-way coupling

The last result showed a small difference between one and two-way coupling computations. In order to quantify this difference for other mass loadings, five cases with ϕ equals to: 0.013, 0.25, 0.5, 1.0 and 1.5 were simulated and its contours are shown in Fig. 32. Once again, no major modification in the penetration ratio is observed due to the mass loading variation but its magnitude is slowly increasing as the mass loading became higher.

Figure 33 presents the penetration ratio profile for each mass loading above mentioned. As the mass loading increases, notable increase in regions between 70° and 115° are seen. A similar behavior has been observed in direct numerical simulation by Bosse, Kleiser e Meiburg (2006). In two-way coupled simulations, the mechanism responsible for the particle velocity enhancement can be explained by three contributing effects. The first one is the inertia which forces particles to accumulate in regions of high strain and low vorticity. The second effect, usually known as preferential sweeping, happens because the gravity is present. Its presence cause the particles to travel primarily toward regions of

downward fluid motion. Finally, the third effect is a local modification of the fluid velocity structure by the particles in regions of increased particle concentration.

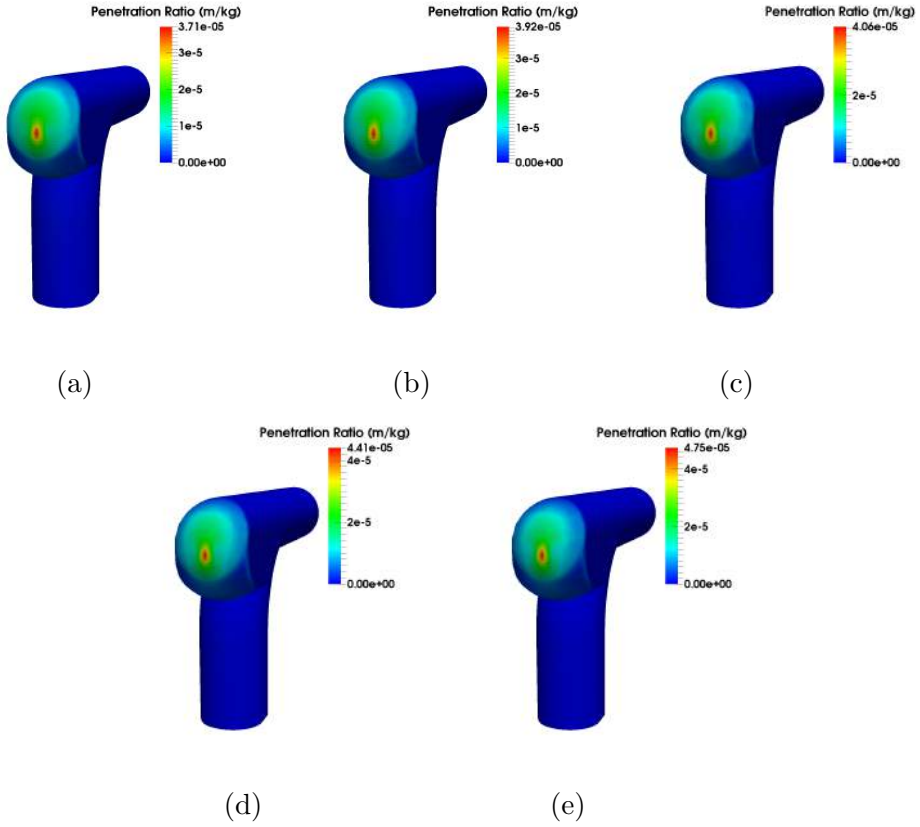

Figure 32 – Erosion contours with two-way coupling approach for the growing mass loadings: (a) $\phi = 0.013$; (b) $\phi = 0.25$; (c) $\phi = 0.5$; (d) $\phi = 1.0$; (e) $\phi = 1.5$.

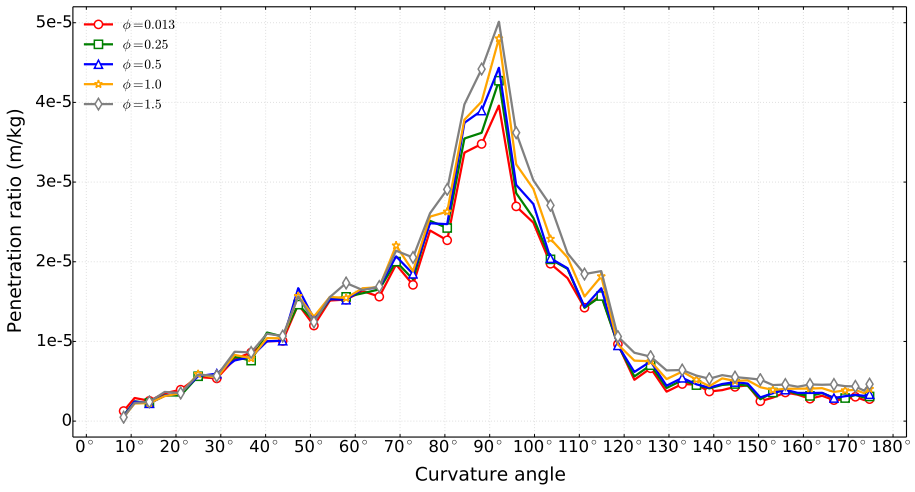

Figure 33 – Numerical penetration ratio versus bend curvature angle with two-way coupling approach for the growing mass loadings: (a) $\phi = 0.013$; (b) $\phi = 0.25$; (c) $\phi = 0.5$; (d) $\phi = 1.0$; (e) $\phi = 1.5$.

As a result, the vertical configuration of the vortex-chamber elbow contributes to guide low mass loading particles to concentrate in low velocity regions (Fig. 27a) faster. As the mass loading increases, it takes longer time to particles reach this regions, forcing them to hit more times in the outer chamber surface. This can explain why the increase of the mass loading is increasing the penetration ratio in two-way coupling.

Figures 34a and 34b shows the "w" mean velocity component of the fluid and particles, respectively. These values were taken from a line in the symmetry plane passing exactly in the center of the vortex chamber and perpendicular to the upward direction of the flow. The mean fluid velocity in this region presents an interesting behavior as the mass loading is increased. The rotative profile is clearly observed for all the mass loading but is perfectly achieved for $\phi = 0.013$. For this mass loading the peak of the velocities are nearly 20 m/s. As the mass loading increases the velocity profiles are attenuated by the loss of momentum due to the presence of more particles in the flow. As a consequence, the mean particles velocity are enhanced (Fig. 34b) affecting the penetration ratio profile.

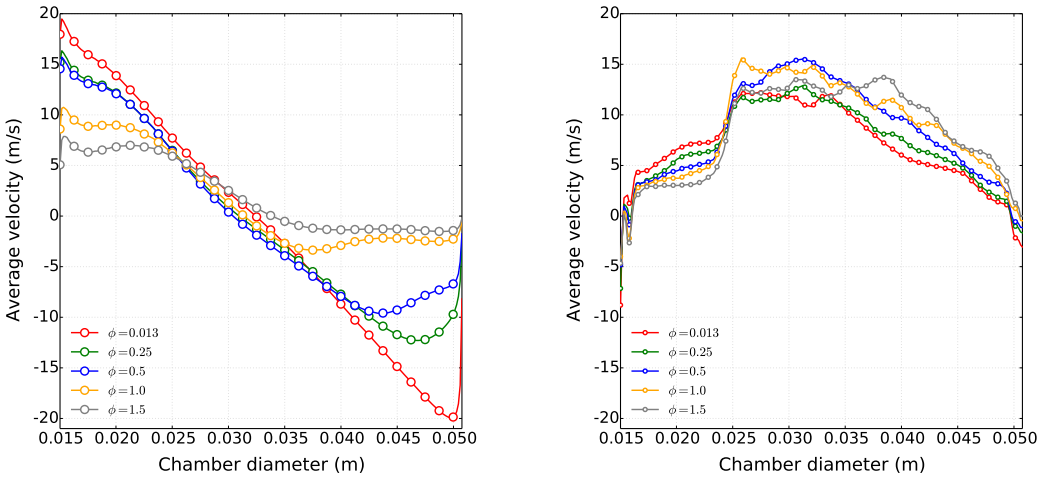

Figure 34 – Average velocity inside the vortex chamber: (a) fluid, (b) particle.

It is important to have in mind that this analyses involves a certain level of complexity due to the nature of the flow and the 3 dimensional effects. The next Section is dedicated to show and explain the penetration ratio profiles when inter-particles collisions are present.

8.2.4 Influence of the mass loading in the penetration ratio - Four-way coupling

In order to investigate the influence of the mass loading, five cases with the same mass loading of the last section were simulated. The difference now is that all the cases considered particle-to-particle collisions. Figure 35 displays the penetration ratio

contours for the five cases studied. The erosion contours shows an extreme reduction of the penetration ratio magnitude from $\phi = 0.013$ to $\phi = 1.5$.

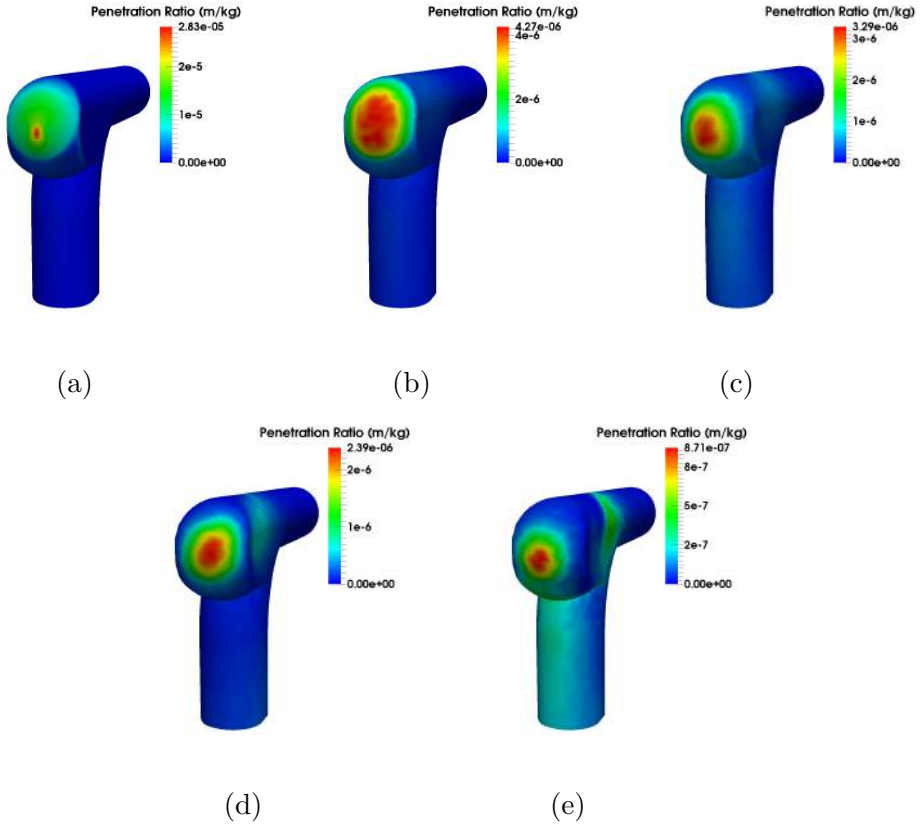

Figure 35 – Erosion contours with four-way coupling approach for the growing mass loadings: (a) $\phi = 0.013$; (b) $\phi = 0.25$; (c) $\phi = 0.5$; (d) $\phi = 1.0$; (e) $\phi = 1.5$.

As expected, inter-particles collision is the most important effect related to the penetration ratio reduction in vortex-chamber elbows. To better visualize the contours of the penetration ratio for each mass loading and understand its impact for each case, the penetration ratio magnitude for $\phi = 1.5$ was fixed and the others mass loading were plotted based o its magnitude (Fig. 36).

For $\phi = 0.013$ (Fig. 36a), practically all the surface of the vortex chamber has higher penetration ratio values compared to $\phi = 1.5$ (Fig. 36e). As the mass loading is increased, the values that exceed the fixed one diminish but secondary regions present erosion effects. The mass loading equals to: $\phi = 0.25$ (Fig. 36b), $\phi = 0.5$ (Fig. 36c), $\phi = 1.0$ (Fig. 36d) and $\phi = 1.5$ (Fig. 36e) shows a new region of penetration ratio. This region is present on the lateral part of the vortex chamber and can not be captured by one and two-way coupling simulations. When four-way coupling is used, while some particles rotates inside the chamber, incoming particles are forced to collide with them in order to prevent direct impact to the vortex chamber wall. This collisions can result in two situations. First, after the collision in the deflection zone the particles returns to main the main core flow and leave without hitting other surfaces. The second situation, which is

probably causing the lateral penetration ratio, is related to the redirection of the particles to the lateral wall. After the collisions, instead of return to core flow, particles are directed to the nearest wall, resulting in the increase of the penetration ratio at this regions.

Although this lateral effect exists, its magnitude does not offer great concern about a new failure location. The penetration ratio at this regions can be neglected compared to the peak observed on the surface of the vortex chamber.

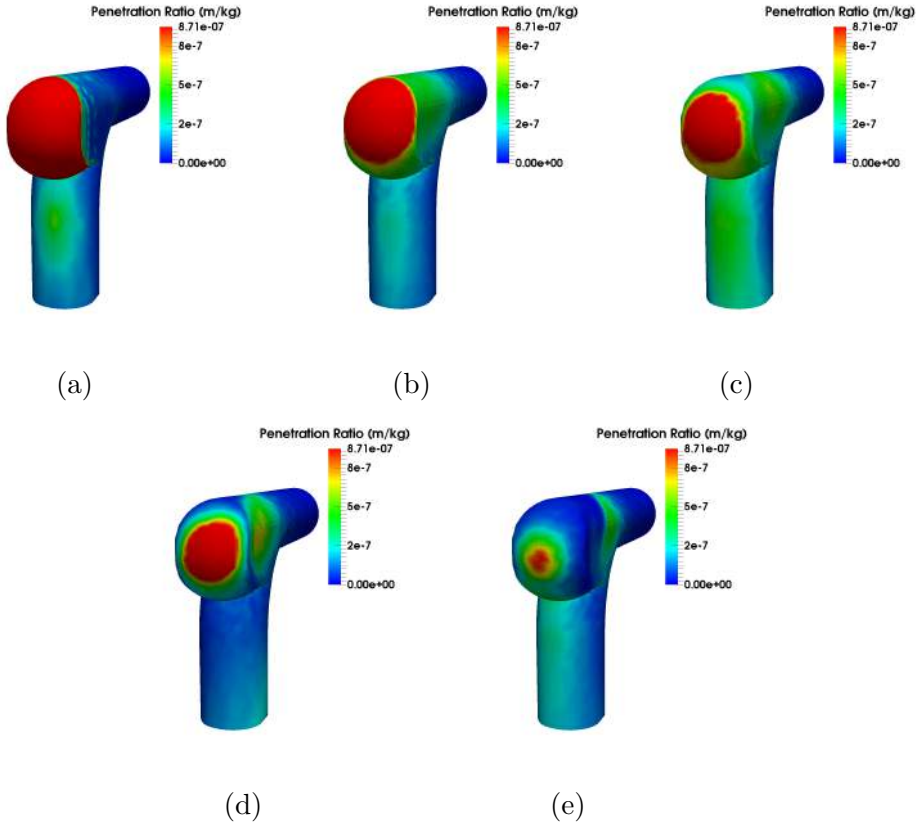

Figure 36 – Erosion contours with four-way coupling approach for the growing mass loadings: (a) $\phi = 0.013$; (b) $\phi = 0.25$; (c) $\phi = 0.5$; (d) $\phi = 1.0$; (e) $\phi = 1.5$ and fixed for $\phi = 1.5$ magnitude.

Finally, the penetration ratio profile for each mass loading is quantitatively presented in Figure 37. This result shows how effective the inter-particle collisions can be. Comparing $\phi = 0.013$ to $\phi = 1.5$ a peak reduction of 96.87 % is obtained. This impressive result shows the capacity of the cushioning effect to reduce erosion wear.

As stated in Section 8.1.3, the abruptly reduction in the peak of the penetration ratio with the mass loading increase, caused by the cushioning effect, is clearly noticed. Once again, this behavior contradicts the common sense, but the vortex chamber structure provides the perfect situation to take advantage of this mechanism.

The next section proposes the mechanisms responsible for the penetration ratio reduction and explains the cushioning effect. In addition, the deflection zone is presented as well as its importance to the erosion reduction.

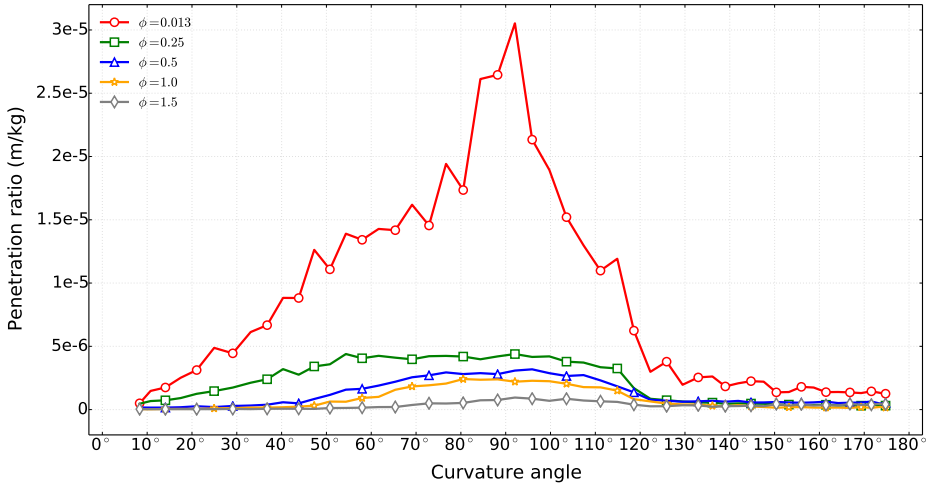

Figure 37 – Numerical penetration ratio versus bend curvature angle with four-way coupling approach for the growing mass loadings: (a) $\phi = 0.013$; (b) $\phi = 0.25$; (c) $\phi = 0.5$; (d) $\phi = 1.0$; (e) $\phi = 1.5$.

8.2.5 Mechanisms of erosion reduction

As mentioned above, the abruptly decrease in the penetration ratio related to the increase of the mass loading occurs in a preferred region of the vortex-chamber elbow between 10° and 120°. In exception of $\phi = 0.013$, the other mass loading simulations have a peculiar behavior between 125° and 175°. It was also confirmed that this behavior is a consequence of the particle-to-particle collisions and will be explained ahead.

Figure 38 shows a symmetry plane of the particle concentration for a mass loading of $\phi = 1.5$ in one (Fig. 38a), two (Fig. 38b) and four-way (Fig. 38c) coupling regimes.

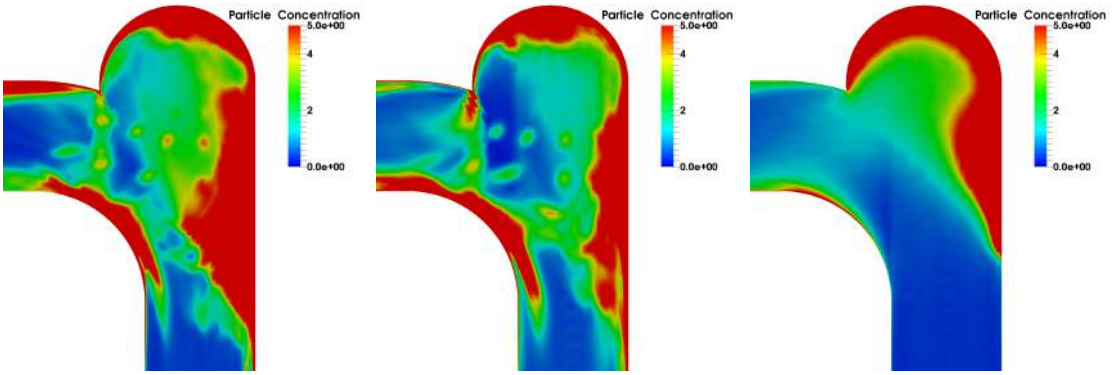

(a) (b) (c)

Figure 38 – Particle concentration field for mass loading $\phi = 1.5$: (a) One-way calculation; (b) Two-way calculation; (c) Four-way calculation.

It can be seen that one and two-way coupling model contours are quite similar. The major difference between them is the enlarged region in one-way approach of the

particle concentration just before the elbow entrance. In one-way coupling the particles are totally driven by the carrier flow, this forces them to travel primarily to regions of low velocity gradients (Fig. 27a) increasing the concentration at these locations (Fig. 38a). When particles feedback on fluid (two-way coupling), this concentration region attenuates but is still present. Even exchanging momentum with the fluid, the particles are carried for low-speed regions and remains there.

When particle-to-particle collisions are included in the model, the above described concentration region is displaced to the vicinity of the vortex chamber. Another visible difference between four-way coupling and the others is the smoothed concentration contour. Two well-defined regions are responsible to the penetration reduction in four-way coupled simulations. First, the convex region just before the vortex chamber, known as the deflection zone. Second, the layer of particles near the surface of the vortex chamber. Before reach the vortex chamber wall, the incoming particles are submitted to both regions and are deflected or cushioned, respectively.

The cushioning effect here is much more effective when compared to the standard elbow but is important to highlight the deflection zone, which is not present in the standard elbow. This explain the rapidly reduction in the penetration observed before (Fig. 37) and gives us an idea of the benefits to combine this two mechanisms.

It is noteworthy that in one and two-way coupling a layer of particles exists near the vortex chamber wall but the absence of inter-particle collisions in the models do not allow a true assessment of the cushioning phenomenon.

8.2.6 Standard elbow versus Vortex-chamber elbow

Finally, Fig. 39 shows the penetration ratio profile of all the mass loadings studied for both elbow types. Such a comparison provides an overview of the complete analyses made in this dissertation and help us understand the benefits of each elbow.

It is clearly seen that even the higher penetration ratio peak of the vortex-chamber elbow is smaller than the lower penetration ratio peak of the standard elbow. This result shows the vortex-chamber elbow potential in reducing the penetration ratio. This efficiency is enhanced as the mass loading is increased. An important conclusion resides in the flow regime, it is known that for high mass loading both elbows reduces the penetration ratio, but, as Fig. 39 reveals, the best situation for the vortex-chamber elbow occurs at high mass loadings. This findings is in accordance with HammerTek Corporation studies case, which affirms that the failure of the vortex-chamber takes at least 10 times longer than the standard elbow under the same operations circumstances.

This is the first time that a CFD tool captured this mechanisms of penetration ratio reduction and exposed the results to the research community. Even with some model

simplifications and using empirical correlations the results are remarkable.

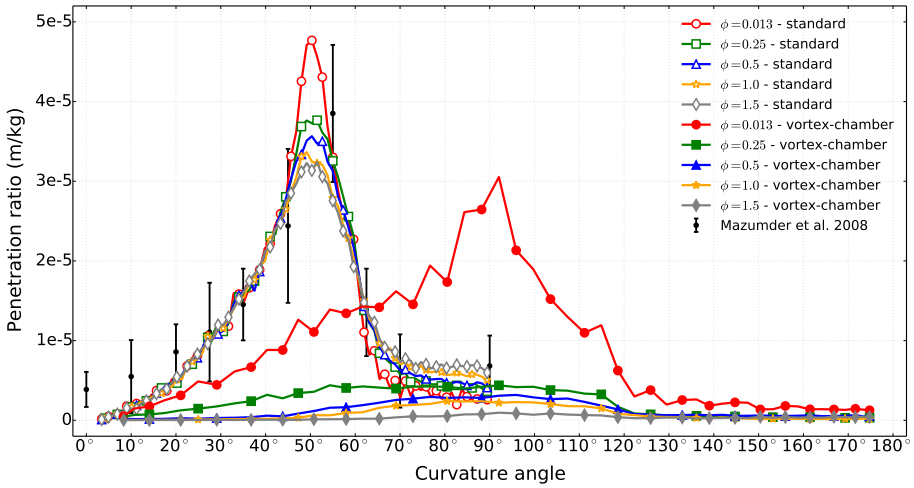

Figure 39 – Comparison between the standard and the vortex-chamber elbows.

Table 3 provides a quantitative comparison of the peak of the penetration ratio reduction for both elbows, obviously, in four-way coupling. The percentage of reduction for $\phi = 1.5$ illustrates the gain for adding a vortex chamber which is approximated 97%. For industrial purpose a reduction of this magnitude can save a lot of money on maintenance. The table also shows that even for smaller mass loadings the vortex chamber proves to be an attractive alternative to the standard elbow.

Table 3 – Standard elbow (SE) and vortex-chamber elbow (VCE) peak reduction.

Mass loading	SE peak (m/kg)	VCE peak (m/kg)	Peak reduction (%)
$\phi = 0.013$	4.767E-5	3.052E-5	35.97
$\phi = 0.25$	3.765E-5	4.392E-6	88.33
$\phi = 0.5$	3.564E-5	3.182E-6	91.07
$\phi = 1.0$	3.365E-5	2.414E-6	92.82
$\phi = 1.5$	3.242E-5	9.522E-7	97.06

These results amongst the results of the rest of the research are concluded in total in the next chapter.

9 Conclusions

The current study has focused on the behavior of erosion in both standard and vortex-chamber elbows. One validation erosion model supported in the creation of a decent simulation setup, after which the resulting setup was employed for simulating the vortex-chamber elbow. The current study has produced a simulation setup that is able to predict erosion phenomena inside pipe fittings with sufficient accuracy. Moreover it has revealed that including the vortex chamber geometry has a positive effect on the penetration ratio reduction.

Below a more elaborate discussion is presented concerning the separate phases in the research, i.e. the standard elbow and the cushioning effect in the validation phase and the vortex-chamber elbow simulations in the analysis phase.

Validation phase

By using accurate CFD models for the gas-particle flow within a ninety-degree-elbow, it was possible to better understand the particle behavior and its consequences on the erosion. A major feature of this validation has been the numerical investigation of the mass loading effects on the erosion ratio.

Based on the simulation results, it can be concluded that even at low mass loadings, the effects of inter-particle collisions on the penetration ratio cannot be disregarded. The main contribution of this work is the prediction and evaluation of the cushioning effect in elbow erosion. It is noteworthy that such effect has been noticed experimentally and can be present in several industrial situations. It may also be the key to understanding erosion-related problems.

The decay of the penetration ratio with increasing the mass loading was found to be due to particle-to-particle collisions. Although this phenomenon may appear as beneficial, it is important to bear in mind that equipment regions not subject to erosion at low particle concentrations might become susceptible at higher concentrations.

Analysis phase

Since many industrial processes requires the transportation of high mass loading, the vortex-chamber elbow appears as a very interesting alternative. Based on the simulation results, it can be concluded that the vortex-chamber elbow show its full potential when dealing with dense phases despite showing efficient for low mass loadings as well.

Due to the excellent agreement of the numerical computations obtained with the

validation phase in combination with all required models for the erosion prediction, it may be concluded that the models presented here are capable for supporting the optimization and the design of pneumatic conveying systems. In addition, with the knowledge of the inter-particles collision effects it will be now also possible to predict erosion rates in the different pipe elements.

The deflecting and cushioning effects demonstrated to be the key in reducing vortex-chamber elbow erosion. With this in mind, this report contributes to the development of new geometries that can benefit from such effects.

Although the research objective is fulfilled, new interesting topics for future research have emerged. The subsequent chapter discusses those topics. Moreover, it provides several illustrations for different simulations.

10 Future research

In the current research it was only possible to study the erosion process isolated. Although the outcome was satisfying, some topics may be interesting for future research. These topics are listed below:

- change the elbows configuration;
- change fluid and particles properties;
- analyze erosion in cyclone separators;
- consider unsteady simulations of the particle-laden flow using Large Eddy Simulations;
- add corrosion models to work alongside with erosion models.

Bibliography

AHLERT, K. *Effects of Particle Impingement Angle and Surface Wetting on Solid Particle Erosion of AISI 1018 Steel*. [S.l.]: University of Tulsa, 1994. Cited 3 times on pages 27, 28, and 48.

ASKELAND, D.; FULAY, P.; WRIGHT, W. *The Science and Engineering of Materials*. [S.l.]: Cengage Learning, 2010. ISBN 9780495296027. Cited on page 22.

BENSON, M.; TANAKA, T.; EATON, J. K. Effects of Wall Roughness on Particle Velocities in a Turbulent Channel Flow. *Journal of Fluids Engineering*, v. 127, n. 2, p. 250–256, dez. 2004. ISSN 0098-2202. Cited on page 39.

BIKBAEV, F. A. et al. Main factors affecting gas abrasive wear of elbows in pneumatic conveying pipes. *Chemical and Petroleum Engineering*, v. 9, n. 1, p. 35–36, 1979. Cited on page 62.

BOSSE, T.; KLEISER, L.; MEIBURG, E. Small particles in homogeneous turbulence: Settling velocity enhancement by two-way coupling. *Physics of Fluids (1994-present)*, v. 18, n. 2, p. –, 2006. Cited on page 70.

BOUSSINESQ, J. *Essai sur la théorie des eaux courantes*. [S.l.]: Imprimerie Nationale, 1877. (Mémoires présentés par divers savants à l'Académie des sciences de l'Institut national de France). Cited on page 34.

BREUER, M.; ALLETTO, M.; LANGFELDT, F. Sandgrain roughness model for rough walls within eulerian–lagrangian predictions of turbulent flows. *International Journal of Multiphase Flow*, v. 43, n. 0, p. 157 – 175, 2012. ISSN 0301-9322. Cited on page 38.

CHEN, X.; MCLAURY, B. S.; SHIRAZI, S. A. Application and experimental validation of a computational fluid dynamics (cfd)-based erosion prediction model in elbows and plugged tees. *Computers & Fluids*, v. 33, n. 10, p. 1251 – 1272, 2004. ISSN 0045-7930. Cited on page 27.

CHEN, X.; MCLAURY, B. S.; SHIRAZI, S. A. Numerical and experimental investigation of the relative erosion severity between plugged tees and elbows in dilute gas/solid two-phase flow. *Wear*, v. 261, n. 7–8, p. 715 – 729, 2006. ISSN 0043-1648. Cited on page 27.

CROWE, C.; MICHAELIDES, E.; SCHWARZKOPF, J. *Multiphase Flow Handbook*. [S.l.]: Taylor & Francis, 2005. (Mechanical and Aerospace Engineering Series). ISBN 9781420040470. Cited on page 38.

CROWE, C. et al. *Multiphase Flows with Droplets and Particles*. [S.l.]: Taylor & Francis, 1997. ISBN 9780849394690. Cited on page 38.

DENNIS, S. C. R.; SINGH, S. N.; INGHAM, D. B. The steady flow due to a rotating sphere at low and moderate reynolds numbers. *Journal of Fluid Mechanics*, v. 101, p. 257–279, 11 1980. ISSN 1469-7645. Cited on page 37.

DESHPANDE, N.; BARIGOU, M. The flow of gas–liquid foams through pipe fittings. *International Journal of Heat and Fluid Flow*, v. 22, n. 1, p. 94 – 101, 2001. ISSN 0142-727X. Cited on page 25.

DUARTE, C. A. R.; SOUZA, F. J. de; dos Santos, V. F. Numerical investigation of mass loading effects on elbow erosion. *Submitted to Powder Technology - Ref. No.: ??*, Elsevier, 2015. Cited on page 40.

ELGHOBASHI, S. On predicting particle-laden turbulent flows. *Applied Scientific Research*, Kluwer Academic Publishers, v. 52, n. 4, p. 309–329, 1993. ISSN 0003-6994. Cited on page 49.

FERZIGER, J. H.; PERIC, M. *Computational methods for fluid dynamics*. [S.l.]: Springer, 2002. Cited 4 times on pages 43, 44, 46, and 47.

FINNIE, I. Erosion of surfaces by solid particles. *Wear*, v. 3, n. 2, p. 87 – 103, 1960. ISSN 0043-1648. Cited 2 times on pages 22 and 23.

FORDER, A.; THEW, M.; HARRISON, D. A numerical investigation of solid particle erosion experienced within oilfield control valves. *Wear*, v. 216, n. 2, p. 184 – 193, 1998. ISSN 0043-1648. Cited 2 times on pages 30 and 48.

FRöHLICH, J.; TERZI, D. von. Hybrid les/rans methods for the simulation of turbulent flows. *Progress in Aerospace Sciences*, v. 44, n. 5, p. 349 – 377, 2008. ISSN 0376-0421. Cited 2 times on pages 9 and 32.

GAHR, K. Z. *Microstructure and Wear of Materials*. [S.l.]: Elsevier, 1987. v - vi p. (Tribology Series, v. 10). ISSN 0167-8922. Cited on page 22.

GRANT, G.; TABAKOFF, W. Erosion Prediction in Turbomachinery Resulting from Environmental Solid Particles. *Journal of Aircraft*, American Institute of Aeronautics and Astronautics, v. 12, n. 5, p. 471–478, maio 1975. ISSN 0021-8669. Cited 5 times on pages 30, 40, 41, 48, and 56.

GUIDE, F. *Fluent 6.2 User Guide*. Centerra Resource Park, 10 Cavendish Court, Lebanon, NH 03766, USA, 2005. Cited on page 43.

HASELBACHER, A.; NAJJAR, F.; FERRY, J. An efficient and robust particle-localization algorithm for unstructured grids. *Journal of Computational Physics*, v. 225, n. 2, p. 2198 – 2213, 2007. ISSN 0021-9991. Cited 2 times on pages 39 and 51.

HUMPHREY, J. Fundamentals of fluid motion in erosion by solid particle impact. *International Journal of Heat and Fluid Flow*, v. 11, n. 3, p. 170 – 195, 1990. ISSN 0142-727X. Cited 2 times on pages 9 and 24.

HUTCHINGS, I. M. *Tribology: friction and wear of engineering materials*. [S.l.]: Edward Arnold, 1992. (Metallurgy and materials science). Cited 2 times on pages 22 and 23.

JONES, W.; LAUNDER, B. The prediction of laminarization with a two-equation model of turbulence. *International Journal of Heat and Mass Transfer*, v. 15, n. 2, p. 301 – 314, 1972. ISSN 0017-9310. Cited on page 34.

LAIN, S.; SOMMERFELD, M.; KUSSIN, J. Experimental studies and modelling of four-way coupling in particle-laden horizontal channel flow. *International Journal of Heat and Fluid Flow*, v. 23, n. 5, p. 647 – 656, 2002. ISSN 0142-727X. Cited on page 39.

LAíN, S.; SOMMERFELD, M. Numerical calculation of pneumatic conveying in horizontal channels and pipes: Detailed analysis of conveying behaviour. *International Journal of Multiphase Flow*, v. 39, n. 0, p. 105 – 120, 2012. ISSN 0301-9322. Cited 2 times on pages 49 and 60.

LAíN, S.; SOMMERFELD, M. Characterisation of pneumatic conveying systems using the euler/lagrange approach. *Powder Technology*, v. 235, n. 0, p. 764 – 782, 2013. ISSN 0032-5910. Cited 5 times on pages 9, 27, 49, 50, and 60.

LAUNDER, B.; SHARMA, B. *Application of the Energy-dissipation Model of Turbulence to the Calculation of Flow Near a Spinning Disc*. [S.l.]: Imperial College of Science and Technology, Department of Mechanical Engineering, 1974. Cited on page 34.

LEVEQUE, R. J. Finite-volume methods for non-linear elasticity in heterogeneous media. *International Journal for Numerical Methods in Fluids*, John Wiley & Sons, Ltd., v. 40, n. 1-2, p. 93–104, 2002. ISSN 1097-0363. Cited on page 43.

LUN, C.; LIU, H. Numerical simulation of dilute turbulent gas-solid flows in horizontal channels. *International Journal of Multiphase Flow*, v. 23, n. 3, p. 575 – 605, 1997. ISSN 0301-9322. Cited on page 37.

MATHUR, S. R.; MURTHY, J. Y. A pressure-based method for unstructured meshes. *Numerical Heat Transfer, Part B: Fundamentals*, v. 31, n. 2, p. 195–215, 1997. Cited 2 times on pages 43 and 45.

MAZUMDER, Q. H.; SHIRAZI, S. A.; MCLAURY, B. Experimental investigation of the location of maximum erosive wear damage in elbows. *Journal of Pressure Vessel Technology*, v. 130, n. 1, p. 1–7, 2008. ISSN 00949930. Cited 4 times on pages 27, 52, 57, and 67.

MEI, R. An approximate expression for the shear lift force on a spherical particle at finite reynolds number. *International Journal of Multiphase Flow*, v. 18, n. 1, p. 145 – 147, 1992. ISSN 0301-9322. Cited on page 37.

MILLS, D. *Pneumatic conveying design guide*. 2nd. ed. Burlington: Elsevier, 2004. ISBN 0 7506 5471 6. Cited 3 times on pages 17, 25, and 62.

NEILSON, J.; GILCHRIST, A. Erosion by a stream of solid particles. *Wear*, v. 11, n. 2, p. 111 – 122, 1968. ISSN 0043-1648. Cited 3 times on pages 27, 28, and 48.

OESTERLE, B.; PETITJEAN, A. Simulation of particle-to-particle interactions in gas solid flows. *International Journal of Multiphase Flow*, v. 19, n. 1, p. 199 – 211, 1993. ISSN 0301-9322. Cited on page 39.

OKA, Y.; OKAMURA, K.; YOSHIDA, T. Practical estimation of erosion damage caused by solid particle impact: Part 1: Effects of impact parameters on a predictive equation. *Wear*, v. 259, n. 1–6, p. 95 – 101, 2005. ISSN 0043-1648. 15th International Conference on Wear of Materials. Cited on page 27.

OKA, Y.; OKAMURA, K.; YOSHIDA, T. Practical estimation of erosion damage caused by solid particle impact: Part 2: Mechanical properties of materials directly associated with erosion damage. *Wear*, v. 259, n. 1–6, p. 102 – 109, 2005. ISSN 0043-1648. 15th International Conference on Wear of Materials. Cited 4 times on pages 27, 40, 41, and 48.

PARISHER, R. A.; RHEA, R. A. Chapter 3 - pipe fittings. In: PARISHER, R. A.; RHEA, R. A. (Ed.). *Pipe Drafting and Design (Second Edition)*. Second edition. Woburn: Gulf Professional Publishing, 2002. p. 13 – 47. ISBN 978-0-7506-7439-3. Cited on page 25.

PATANKAR, S. *Numerical Heat Transfer and Fluid Flow*. [S.l.]: Taylor & Francis, 1980. (Series in computational methods in mechanics and thermal sciences). ISBN 9780891165224. Cited on page 46.

PAULSON, J.; HESS, L. *Short radius, low wear elbow*. Google Patents, 1983. US Patent 4,387,914. Disponível em: <http://www.google.com/patents/US4387914>. Cited on page 26.

PENG, K. et al. An improved known vicinity algorithm based on geometry test for particle localization in arbitrary grid. *Journal of Computational Physics*, v. 228, n. 24, p. 9001 – 9019, 2009. ISSN 0021-9991. Cited on page 50.

PEREIRA, G. C.; SOUZA, F. J.; MORO, D. A. Numerical prediction of the erosion due to particles in elbows. *Powder Technology*, Elsevier, v. 261, p. 105–117, 2014. Cited 3 times on pages 23, 24, and 40.

REYNOLDS, O. On the dynamical theory of incompressible viscous fluids and the determination of the criterion. *Philosophical Transactions of the Royal Society of London A: Mathematical, Physical and Engineering Sciences*, The Royal Society, v. 186, p. 123–164, 1895. ISSN 0264-3820. Cited on page 33.

ROTA, V. *Vortice Ell Smart Elbow*. Issue 1. RVB 89: [s.n.], 2001. Cited on page 26.

RUBINOW, S. I.; KELLER, J. B. The transverse force on a spinning sphere moving in a viscous fluid. *Journal of Fluid Mechanics*, v. 11, p. 447–459, 11 1961. ISSN 1469-7645. Cited on page 37.

SAFFMAN, P. G. The lift on a small sphere in a slow shear flow. *Journal of Fluid Mechanics*, v. 22, p. 385–400, 6 1965. ISSN 1469-7645. Cited on page 37.

SCHILLER, L.; NAUMANN, Z. A drag coefficient correlation. *Ver. Deutsch. Ing.*, p. 77–318, 1935. Cited on page 36.

SOMMERFELD, M. Validation of a stochastic lagrangian modelling approach for inter-particle collisions in homogeneous isotropic turbulence. *International Journal of Multiphase Flow*, v. 27, n. 10, p. 1829 – 1858, 2001. ISSN 0301-9322. Cited 2 times on pages 36 and 39.

SOMMERFELD, M.; HUBER, N. Experimental analysis and modelling of particle-wall collisions. *International Journal of Multiphase Flow*, v. 25, n. 6–7, p. 1457 – 1489, 1999. ISSN 0301-9322. Cited 3 times on pages 30, 39, and 48.

SOUZA, F. J. de; SILVA, A.; UTZIG, J. Four-way coupled simulations of the gas-particle flow in a diffuser. *Powder Technology*, v. 253, p. 496–508, 2014. Cited on page 60.

TAKAHASHI, K. et al. Experimental study of low-cycle fatigue of pipe elbows with local wall thinning and life estimation using finite element analysis. *International Journal of Pressure Vessels and Piping*, v. 87, n. 5, p. 211 – 219, 2010. ISSN 0308-0161. Cited on page 27.

TORO, E. *Riemann Solvers and Numerical Methods for Fluid Dynamics: A Practical Introduction*. [S.l.]: Springer, 2009. ISBN 9783540498346. Cited on page 43.

VERSTEEG, H.; MALALASEKERA, W. *An Introduction to Computational Fluid Dynamics: The Finite Volume Method*. [S.l.]: Pearson Education Limited, 2007. ISBN 9780131274983. Cited on page 43.

VIEIRA, R. E. et al. Experimental investigation of the effect of 90 degree standard elbow on horizontal gas–liquid stratified and annular flow characteristics using dual wire-mesh sensors. *Experimental Thermal and Fluid Science*, v. 59, n. 0, p. 72 – 87, 2014. ISSN 0894-1777. Cited 2 times on pages 26 and 27.

WILCOX, D. *Turbulence Modeling for CFD*. [S.l.]: DCW Industries, Incorporated, 1994. ISBN 9780963605108. Cited on page 34.

ZHANG, Y. et al. Comparison of computed and measured particle velocities and erosion in water and air flows. *Wear*, v. 263, n. 1–6, p. 330 – 338, 2007. ISSN 0043-1648. 16th International Conference on Wear of Materials. Cited 3 times on pages 27, 29, and 48.

Appendix

APPENDIX A – Additional illustrations

This appendix provide some illustrations that may be useful to better understand the flow and the particles behavior inside both elbows. These illustrations are listed below.

1. Fig. 40, fluid velocity components of the standard elbow;
2. Fig. 41, pressure and turbulence kinetic energy of the standard elbow;
3. Fig. 42, fluid velocity components of the vortex-chamber elbow;
4. Fig. 43, pressure and turbulence kinetic energy of the vortex-chamber elbow;
5. Fig. 44, particles behavior inside the standard elbow (colored by diameter);
6. Fig. 45, particles behavior inside the standard elbow (colored by rotation);
7. Fig. 46, particles behavior inside the vortex-chamber elbow (colored by diameter);
8. Fig. 47, particles behavior inside the vortex-chamber elbow (colored by rotation).
9. Fig. 48, particles behavior for different coupling regimes (colored by velocity).

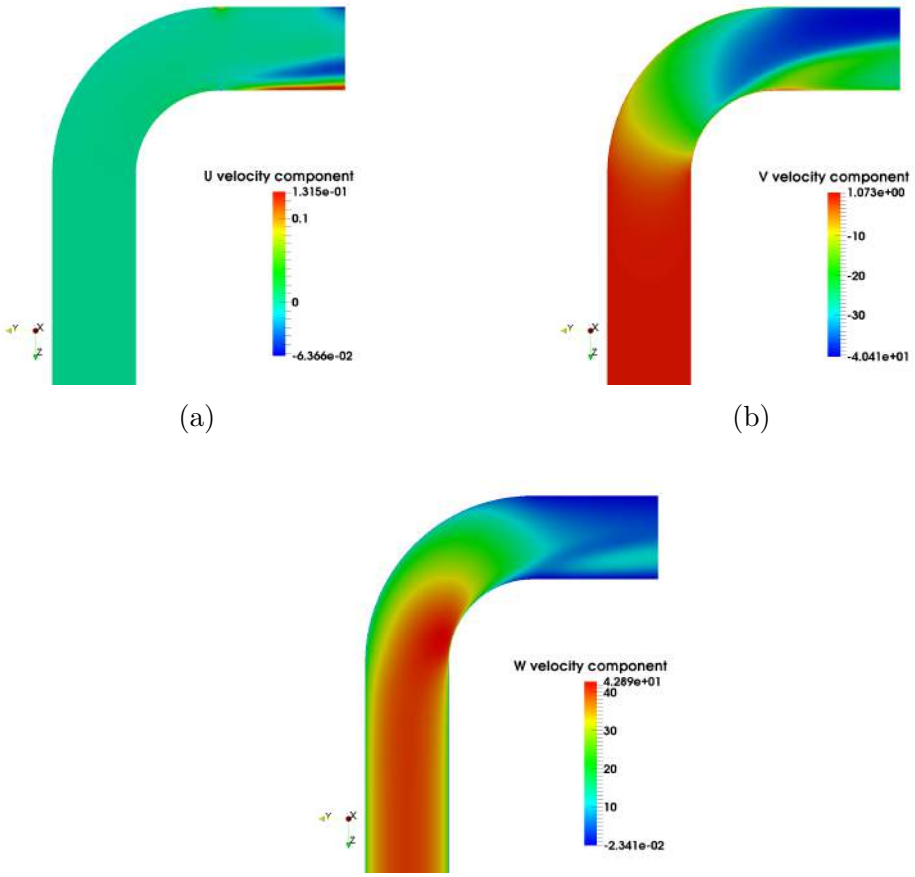

(a) (b)

(c)

Figure 40 – Standard elbow fields: (a) U velocity component; (b) V velocity component; (c) W velocity component.

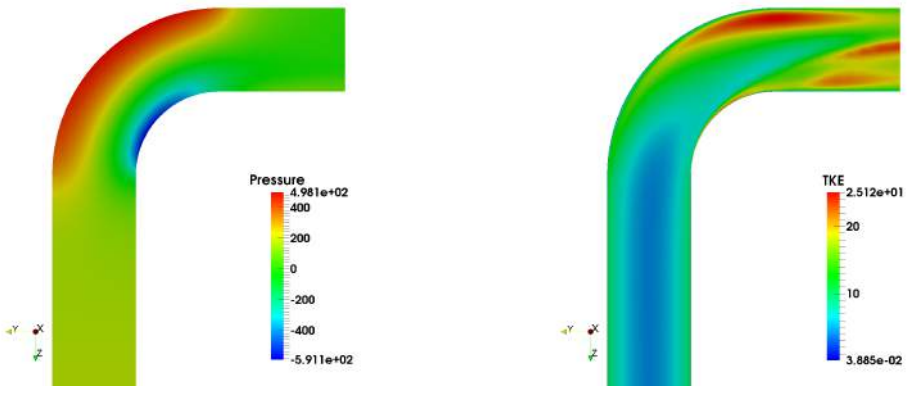

(a) (b)

Figure 41 – Standard elbow fields: (a) Pressure; (b) Turbulence Kinetic Energy.

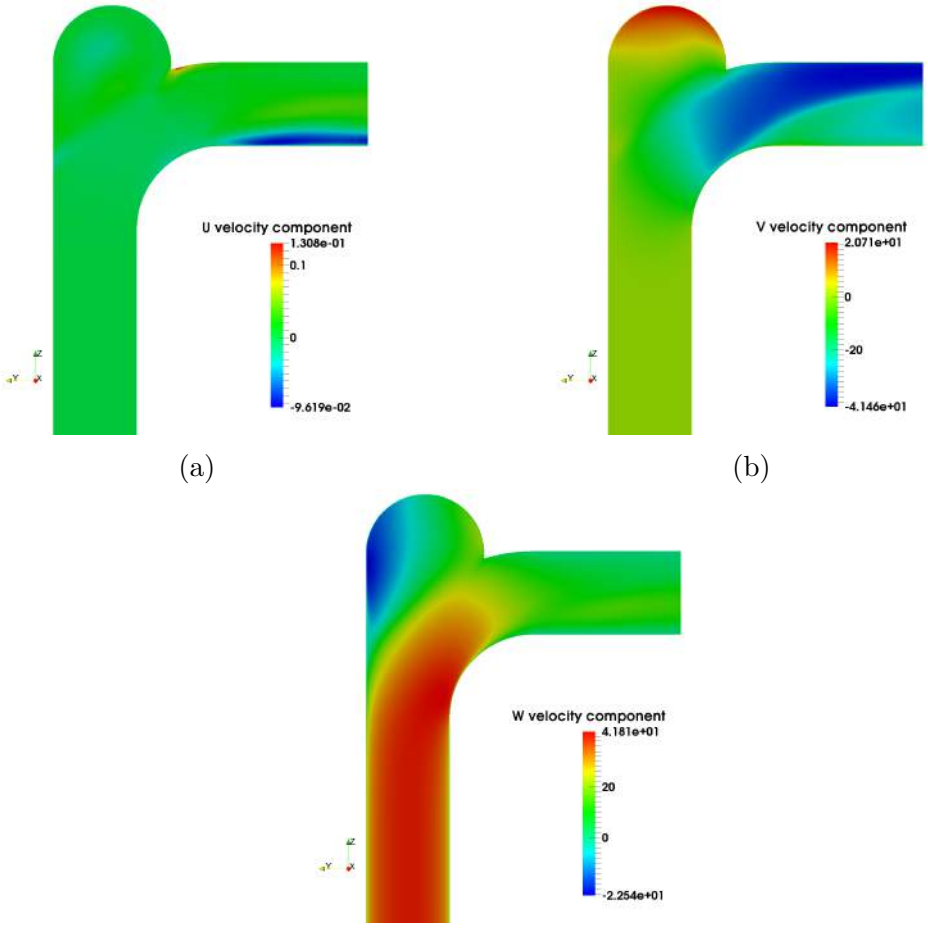

(a) (b)

(c)

Figure 42 – Vortex-chamber elbow fields: (a) U velocity component; (b) V velocity component; (c) W velocity component.

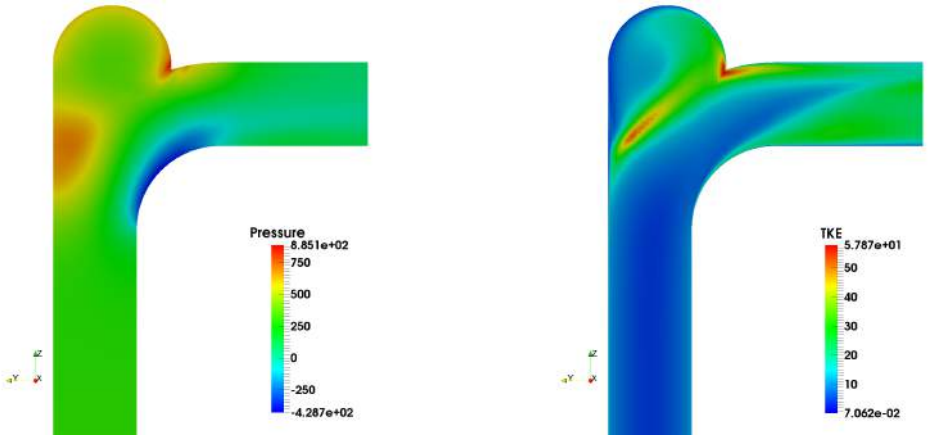

(a) (b)

Figure 43 – Vortex-chamber elbow fields: (a) Pressure; (b) Turbulence Kinetic Energy.

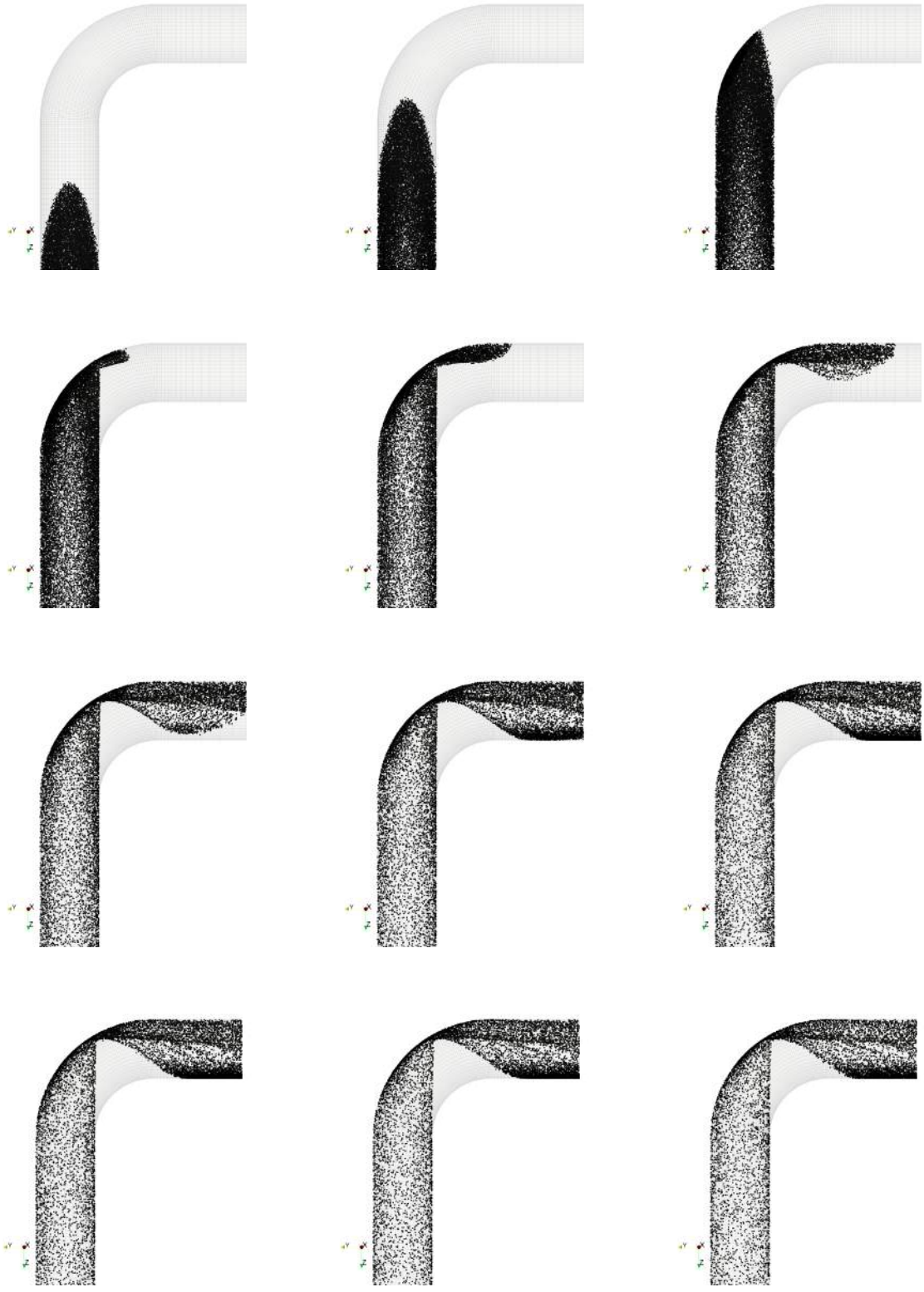

Figure 44 – Snapshot of particle behavior inside the standard elbow colored by diameter (one-way coupling).

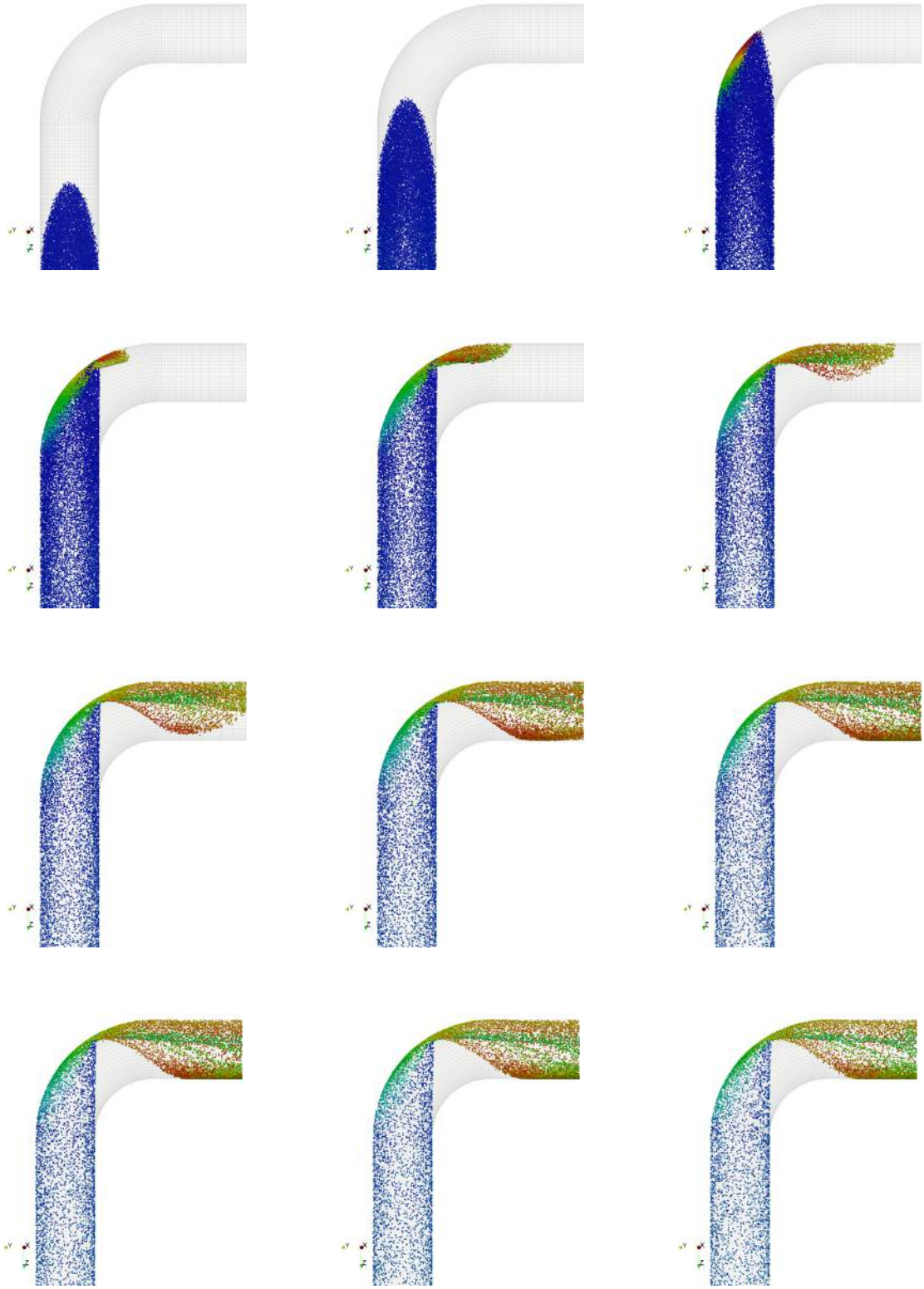

Figure 45 – Snapshot of particle behavior inside the standard elbow colored by rotation: blue - low, red - high (one-way coupling).

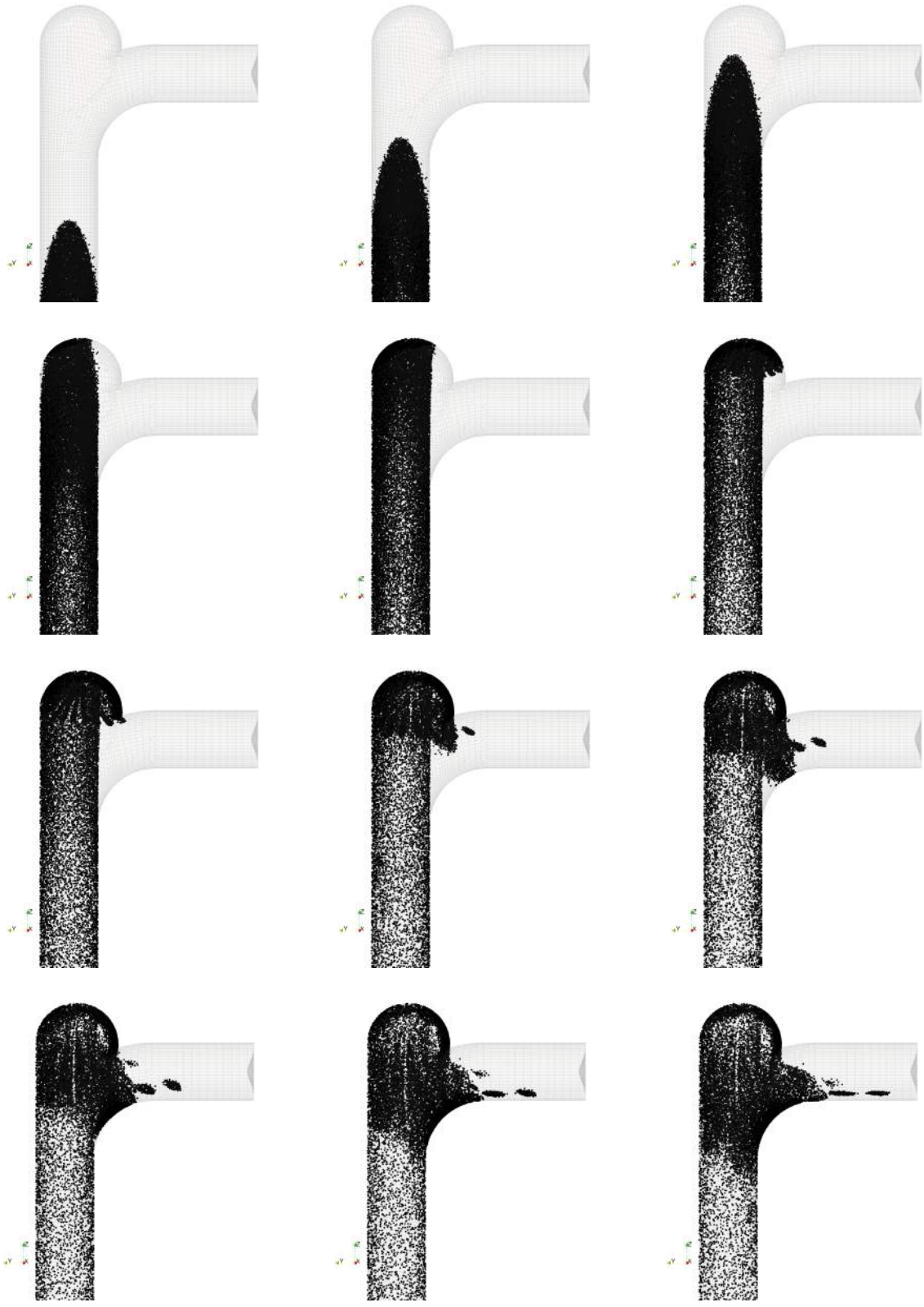

Figure 46 – Snapshot of particle behavior inside the vortex-chamber elbow colored by diameter (one-way coupling).

Figure 47 – Snapshot of particle behavior inside the vortex-chamber elbow colored by rotation: blue - low, red - high (one-way coupling).

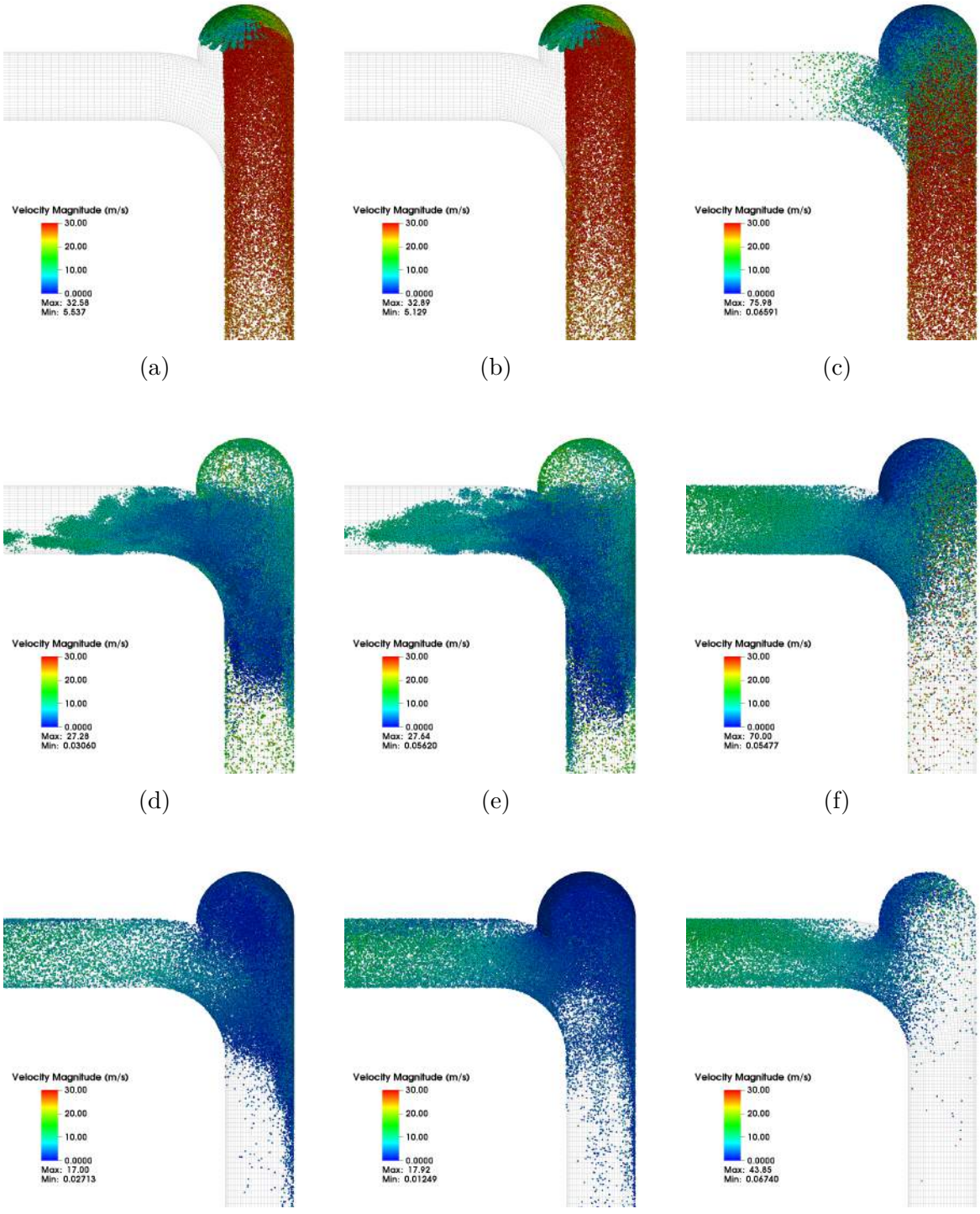

Figure 48 – Snapshot of particles behavior for $\phi = 1.0$. From top to bottom: 0.39s, 0.5s and 0.8s. From left to right: one-way, two-way and four-way coupling.